University of South Florida
Scholar Commons

Graduate Theses and Dissertations | Graduate School

10-29-2009

Investigation of Residual and Thermal Stress on Membrane-Based MEMS Devices

Lynford O. Davis
University of South Florida

Follow this and additional works at: https://scholarcommons.usf.edu/etd

Part of the American Studies Commons

Scholar Commons Citation

Davis, Lynford O., "Investigation of Residual and Thermal Stress on Membrane-Based MEMS Devices" (2009). *Graduate Theses and Dissertations.*
https://scholarcommons.usf.edu/etd/1925

This Thesis is brought to you for free and open access by the Graduate School at Scholar Commons. It has been accepted for inclusion in Graduate Theses and Dissertations by an authorized administrator of Scholar Commons. For more information, please contact scholarcommons@usf.edu.

www.manaraa.com

Investigation of Residual and Thermal Stress on Membrane-Based MEMS Devices

by

Lynford O. Davis

A thesis submitted in partial fulfillment
of the requirements for the degree of
Master of Science in Mechanical Engineering
Department of Mechanical Engineering
College of Engineering
University of South Florida

Major Professor: Rasim Guldiken, Ph.D.
Ashok Kumar, Ph.D.
Muhammad Rahman, Ph.D.

Date of Approval:
October 29, 2009

Keywords: Film stress, PECVD, Radius of curvature, Deflection, CMUT

© Copyright 2009, Lynford O. Davis

المنارة للاستشارات

www.manaraa.com

DEDICATION

I would like to dedicate this thesis to my parents Lynford I. Davis and Olga M. Davis, and to my sister Natalie Davis, who have inspired me in many ways. This work would not have been possible without their prayers, support, and confidence in me throughout my years of college.

المنارة للاستشارات

www.manaraa.com

ACKNOWLEDGEMENTS

I would like to thank my advisor Rasim Guldiken for his guidance and insight that helped me in this work. I would also like to thank Mr. Robert Tufts and Mr. Richard Everly who are engineers at the Nanomaterials and Nanomanufacturing Research Center (NNRC) at the University of South Florida for their continuous help and expert advice throughout my research. I would like to especially thank Dr. Rahman and Dr. Kumar for serving on my thesis committee and providing valuable feedback which helped me finalize this manuscript. Most importantly, I would like to thank my fiancée Veronica for her patience and support for me during my time as a graduate student.

المنارة للاستشارات

www.manaraa.com

TABLE OF CONTENTS

LIST OF TABLES iii

LIST OF FIGURES iv

ABSTRACT vii

CHAPTER 1: INTRODUCTION 1
1.1 Background and Motivation 1
1.2 Silicon Nitride Thin Films 3
1.3 Thin Film Stress 4
1.4 Governing Equations for Stress in Thin Films 5
1.5 Conclusion and Chapter Objectives 9

CHAPTER 2: PROCESSING OF LOW-STRESS SILICON NITRIDE THIN FILMS 10
2.1 Plasma Enhanced Chemical Vapor Deposition (PECVD) Process 10
2.1.1 Plasma 10
2.1.2 Chemical Vapor Deposition (CVD) 11
2.1.3 Plasma Enhanced Chemical Vapor Deposition (PECVD)............. 11
2.2 Wafer Preparation and Silicon Nitride Deposition 13
2.3 Silicon Nitride Film Thickness Measurement 14
2.4 Residual Film Stress Measurement..16
2.5 Accuracy of Method Used to Determine Film Stress 25

CHAPTER 3: SILICON NITRIDE FILM CHARACTERIZATION..............................27
3.1 Overview of Data Collected 27
3.2 Effect of RF Power..28
3.3 Effect of Deposition Time 31
3.4 Effect of Nitrogen Flow Rate..32
3.5 Effect of Pressure 36
3.6 Plasma Etch: Overview of Process 36
3.7 Etch Rate Comparison..38

CHAPTER 4: THERMAL STRESS EFFECTS IN MULTI-LAYER MEMS STRUCTURES 41
4.1 Overview of Thermal Stress in Thin Films 41

المنارة للاستشارات

www.manaraa.com

4.2 Background Equations on Thermal Stress in Thin Films 42
4.3 Background Equations on Center Deflection in a MEMS Structure 43
4.4 Analysis of Center-Deflection in Multi-layer MEMS Devices Due to Thermal Stress 45
4.5 Center Deflection in a Three-layer System... 48
4.6 Analytical Modeling of a Three-layer Nitride-Metal-Nitride Membrane 51
4.6.1 Center Deflection and Thickness of Nitride Layer 52
4.6.2 Effect of Metal Electrode Thickness on Membrane Center Deflection 53
4.6.3 Effect of Thermal Expansion Coefficient on Center Deflection 55
4.6.4 Thermal Expansion Coefficient with Normalized Electrode Thickness... 58
4.7 Curvature of a Thin Film on a Substrate Versus a Three-layer Membrane 60
4.8 Conclusion 64

CHAPTER 5: APPLICATIONS OF MEMBRANE-BASED MEMS DEVICES 65
5.1 Overview 65
5.2 Common Membrane-based MEMS Devices 65
5.2.1 MEMS Inertial Sensors 65
5.2.2 MEMS Micro-mirrors 66
5.2.3 MEMS Micro-switch and Micro-Resonators 68
5.2.4 MEMS Rotary Micro-motor.. 69
5.2.5 MEMS Linear Micro-motors... 71
5.2.6 MEMS Micro-grippers.. 72
5.3 Micro-machined Ultrasonic Transducers: An Overview 73
5.4 Capacitive Micromachined Ultrasonic Transducers (CMUTs) 74
5.4.1 Background 74
5.4.2 Operation of Capacitive Micromachined Ultrasonic Transducers (CMUTs) 75
5.5 Fabrication of Capacitive Micromachined Ultrasonic Transducers 77
5.6 Future Work... 80

REFERENCES 81

APPENDICES... 89
Appendix A: Sample MathLab® Code used for Calculating Center Deflection 90

المنارة للاستشارات
www.manaraa.com

LIST OF TABLES

Table 3.1 Original PECVD Silicon Nitride Recipe 28

Table 3.2 Modified PECVD Silicon Nitride Recipe with RF Power at 45 W 29

Table 3.3 PECVD Recipe with Modified Deposition Time 31

Table 3.4 Results Obtained when the Deposition Time was Changed to 7 Minutes 32

Table 3.5 Comparison of Original Recipe and the Effect of Reduced N_2 33

Table 3.6 Increasing RF Power with Reduced N_2 Flow Rate 34

Table 3.7 Effect of a Reduced N_2 Flow Rate with Reduced Power and Time 35

Table 3.8 Recipe for Plasma Etch 36

Table 3.9 Samples Used for Plasma Etch 38

Table 3.10 Summary of Etch Rates 39

Table 4.1 Thermal Expansion Coefficient and Resistivity of Different Metal Alternatives for Electrode in the Membrane. 56

Table 4.2 Resistivity and Effective Metal Thickness for some Metal Alternatives. 58

Table 4.3 Thickness and Thin Film Stress of Four Samples Deposited by PECVD 61

المنارة للاستشارات

www.manaraa.com

LIST OF FIGURES

Figure 1.1 Free Body Diagram Showing Bending Moment on a Plate 5

Figure 1.2 Relationship between Bending Strain and Curvature [12] 6

Figure 1.3 Force per Unit Length and Bending Moment per Unit Length
Acting on Thin Film and Substrate 8

Figure 2.1 Plasma Enhanced Chemical Vapor Deposition (PECVD) System
Used to Deposit and Characterize Silicon Nitride Thin Film 12

Figure 2.2 Ellipsometer Used to Measure the Thickness of the Silicon Nitride Film 16

Figure 2.3 Surface Profilometer Used to Measure the Curvature in the Silicon
Substrate and Compute the Film Stress 18

Figure 2.4 Silicon Wafer Mounted on the Surface Profilometer with Three Stops
Used to Restrict Movement of the Wafer 19

Figure 2.5 Scan of a Wafer before Deposition of Silicon Nitride 20

Figure 2.6 Post-deposition Scan of Silicon Wafer with Silicon Nitride Film and
Stress Computed between 15 mm and 25 mm on the Surface of the Wafer 22

Figure 2.7 Post-deposition Scan of Silicon Wafer with Silicon Nitride Film and
Stress Computed between 5 mm and 35 mm on the Surface of the Wafer 23

Figure 2.8 An Example of the Output Obtained From Scanning the Wafer before
and after Deposition of Silicon Nitride and Computing the Residual Stress .. 24

Figure 3.1 Silicon Nitride Film on a Wafer with Region that was Protected with
Captone Tape Clearly Visible after Plasma Etch 37

Figure 3.2 Alpha-Step Profilometer Used to Measure Silicon Nitride Step Height
From One Surface of the Etched Portion of the Nitride Film to the
Un-etched Portion 40

المنارة للاستشارات
www.manaraa.com

Figure 4.1 Negative Center Deflection of a Beam (u_y or δ) with Displacement along a Radius r, from Center 44

Figure 4.2 Schematic of Three-Layer SIN_X-Metal-SIN_X MEMS Structure 49

Figure 4.3(a-d) Thermal Steps of the First Two Layers of the Three-Layer System........50

Figure 4.4 (a) Thermal Steps of the First Two Layers Along with Radius of Curvature, (b-c) the Complete Three-Layer System and its Radius of Curvature 51

Figure 4.5 Center Deflection of a 50 µm Three-Layer System as a Function of Bottom Layer of Silicon Nitride for Different Thicknesses above the Metal Electrode (H3) 53

Figure 4.6 Center Deflection of a 50 µm Membrane as a Function of Metal Electrode Thickness 55

Figure 4.7 Center Deflection as a Function of Different Metal Alternatives with Constant Thickness 57

Figure 4.8 Center Deflection as a Function of the Different Metal Alternatives with Electrode Thickness Normalized for the Metal Electrical Conductivity 60

Figure 4.9 Curvature of Silicon Nitride Film as a Function of its Thickness on a Silicon Substrate 62

Figure 4.10 Curvature of Three-Layer Membrane (H2= 0.12 µm (Al), H3= 0.2 µm) and Single Nitride Layer on a Substrate, as a Function of Bottom Layer Thickness of the Membrane (H1) 63

Figure 5.1 A Micro-accelerometer, ADXL Series, © Analog Devices Inc [38]...............66

Figure 5.2 DLP Projection System with Single DMD Chip, © Texas Instruments Inc [38] 67

Figure 5.3 Digital Micro-mirror Device (DMD), © Texas Instruments Inc [38] 68

Figure 5.4 An Example of a MEMS RF Switch [38] 69

Figure 5.5 Micro-resonators Fabricated at the IEMN University in France [38] 69

Figure 5.6 SEM Image of a Harmonic (“Wobble”) Micro-motor [3], [39]......................70

المنارة للاستشارات
www.manaraa.com

Figure 5.7 Cross-section of a “Wobble” Micro-motor with Heavily-Doped Polysilicon Shield [40] 71

Figure 5.8 Scratch Drive Actuator Used in Self-Assembly of 3D Polysilicon Structure [43] 72

Figure 5.9 Electrostatic Micro-gripper (a) Top View, (b) Cross-sectional View [44]...... 73

Figure 5.10 Schematic of a Single CMUT Transducer Element [80] 76

Figure 5.11 Annular Ring CMUT Fabricated with a Gap to Membrane Aspect Ratio of 1:1000 [81] 76

Figure 5.12 CMUT with Sealed Membrane Designed for Micro-fluidic Application [79] 77

Figure 5.13 Illustration of the Fabrication Process Flow for a CMUT Designed for Immersion Application [34]... 79

المنارة للاستشارات

www.manaraa.com

Investigation of Residual and Thermal Stress on Membrane-Based MEMS Devices

Lynford O. Davis

ABSTRACT

Thin films have become very important in the past years as there is a tremendous increase in the need for small-scale devices. Thin films are preferred because of their electrical, mechanical, chemical, and other unique properties. They are often used for coatings, and in the fabrication of Microelectronic devices and Micro-electro Mechanical Systems (MEMS). Internal (residual) stress always exists when a thin film is employed in the device design. Residual and thermal stresses cause membrane bow, altering the anticipated dynamic response of a membrane-based MEMS design. The device may even become inoperable under the high stresses conditions. As a result, the stresses that act upon the membrane should be minimized for optimum operation of a MEMS device.

In this research, the fabrication process parameters leading to low stress silicon nitride films were investigated. Silicon nitride was deposited using Plasma Enhanced Chemical Vapor Deposition (PECVD) and the residual stresses on these films were determined using a wafer curvature technique. By adjusting the silane (SiH_4) and nitrogen (N_2) gas flow rates, and the radiofrequency (RF) power; high quality silicon nitride films with residual stress as low as 11 MPa were obtained.

المنارة للاستشارات
www.manaraa.com

Furthermore, an analytical study was also conducted to explore the effect of thermal stresses between layers of thin films on the MEMS device operation. In this thesis, we concentrated our efforts on three layers of thin films, as that is the most commonly encountered in a membrane based MEMS device. The results obtained from a parametric study of the membrane center deflection indicate that the deflection can be minimized by the appropriate choice of materials used. In addition, our results indicate that thin films with similar coefficient of thermal expansion should be employed in the design to minimize the deflection of the membrane, leading to anticipated device operation and increased yield.

A complete understanding of the thermal and residual stress in MEMS structures can improve survival rate during fabrication, thereby increasing yield and ultimately reducing the device cost. In addition, reliability, durability, and overall performance of membrane-based structures are improved when substrate curvature and membrane deflection caused by stresses are kept at a minimum.

المنارة للاستشارات
www.manaraa.com

CHAPTER 1: INTRODUCTION

1.1 Background and Motivation

Micro-electromechanical systems (MEMS) combine sensing and actuation mechanisms, signal processing, control, wireless and optical communication, and power generation on a single system [1]. There are many membrane-based MEMS devices such as: accelerometers, electrostatic RF switches, resonators, micro-motors and capacitive micro-machined ultrasonic transducers (CMUTs).

In MEMS devices such as the CMUTs, the width of a membrane is typically 50-100 μm while the gap height is on the order of 0.1 μm to maximize the device efficiency. Hence, the aspect ratio of these MEMS devices is as high as 1:1000. Note that the initial membrane bow as little as 0.01 degrees puts the membrane in contact with the bottom substrate, making the device inoperable. Hence, one needs to account for all possible initial membrane deflection contributors in the design for proper device operation. It is important to note that all the derived analytical formulations, even simulation studies (unless explicitly stated), assumes an initial flat membrane shape. This contributes to unexpected measured device response as compared to simulated or calculated response.

There are three main factors that cause a membrane-based structure to bow. These are: (1) residual stress developed during the deposition, (2) the effect of atmospheric pressure on the membrane (constant ~0.1MPa), and (3) thermal stress contribution during

المنارة للاستشارات
www.manaraa.com

deposition. In this thesis, we will minimize the residual stress in the Plasma Enhanced Chemical Vapor Deposition (PECVD) reactor by adjusting the process parameters such the silane (SiH_4) and nitrogen (N_2) gas flow rates, and the RF power. Our experimental studies to optimize the gas flow rates and RF power indicate tensile stress as low as 11 MPa in the silicon nitride films, which is considered very low for membrane-based MEMS devices. The second cause is the pressure difference between the gap (vacuum) and the atmosphere. Hence there is a pressure of 0.1 MPa on the membrane at all times. This can bow down the membrane significantly depending on the membrane thickness. As this is a constant force on the membrane, basic analytical or simulation studies can handle this contributor without any difficulty. The third and mostly unknown contributor is the thermal stress in the membrane. The thermal analysis may explain the discrepancy between the experimental membrane deflection results to the simulated results during the design stage. In this thesis, we will illustrate that for most of the membrane thicknesses; the thermal stress is the leading factor for the initial membrane deflection. In this study, we will also derive an analytical formula for 3 layer structures (which is the most commonly encountered configuration for membrane-based MEMS structures) and plot against several membrane variables.

The main research objective of this thesis is to present a clear analysis of the effects of both thermal and residual stress as it is applied to devices that possess a membrane-like structure.

المنارة للاستشارات
www.manaraa.com

1.2 Silicon Nitride Thin Films

Silicon nitride thin film is a widely used material in the micro-fabrication industry [1-3]. It has desirable mechanical and electrical properties such as a high resistivity, high relative permittivity, and high fracture toughness [3]. In addition, silicon nitride is biocompatible and has a high wear resistance. Silicon nitride has a large dielectric constant and can therefore be used in many applications such as a dielectric material in MEMS capacitors [4]. Silicon nitride can be used for passivation, mechanical protection, and as a masking layer for selective oxidation and dry etching [5-6]. Low-stress silicon nitride can be critical to the proper functioning of a MEMS device. In micro-fabrication, thin films are normally deposited using high temperature (greater than 700 degrees centigrade) deposition techniques. Thin films such as silicon nitride, deposited using these methods can result in very high internal stresses. These internal stresses, when coupled with other edge, surface, or bulk imperfections, on a silicon wafer can cause concentrated stresses which can reduce the apparent strength and performance of a MEMS component or device [7].

In this research, low stress silicon nitride thin films were deposited using a PECVD system. The PECVD system was chosen because of its ability to deposit thin film at relatively low temperature (less than 350 degrees centigrade) without compromising the quality of the film [5], [8]. Some parameters that can aid in determining the quality of the deposited film are the film thicknesses, the residual film stress, selectivity to etching, refractive index, etch rate, and surface smoothness [8-10].

المنارة للاستشارات
www.manaraa.com

Previous work has shown that by adjusting the flow rate of the PECVD reactant gases, and the RF plasma power; high-quality, low-stress silicon nitride films can be produced [8], [10-11]. In this project, the main parameters that were used to control the stress in the silicon nitride thin film were the RF plasma power, and the flow rates of silane (SiH_4) and nitrogen (N_2) gases. The quality of the silicon nitride film will be determined based on the magnitude of the residual stress in the film, the refractive index, and the dry etch rate.

1.3 Thin Film Stress

The formation of a thin film typically takes place at an elevated temperature, and the film growth gives rise to thin film stress.

The two main components that lead to internal or residual stresses in thin films are thermal stresses and intrinsic stresses. Thermal stresses are due to strain misfits as a result of differences in the temperature dependent coefficient of thermal expansion between the thin film and a substrate material such as silicon. Intrinsic stresses are due to strain misfits encountered during phase transformation in the formation of a solid layer of thin film [1]. Residual or internal thin film stress therefore can be defined as the summation of the thermal and intrinsic thin film stress components [1]:

$$\sigma_R = \sigma_T + \sigma_I \tag{1}$$

Where:

σ_R is the residual thin film stress

المنارة للاستشارات
www.manaraa.com

σ_T is the thermal stress component

σ_I is the intrinsic stress component

1.4 Governing Equations for Stress in Thin Films

Between a film and a substrate, stress is mainly caused by incompatibilities, or misfits due to differences in thermal expansion, phase transformations with volume changes, and densification of the film [1]. Simple mechanics of materials solutions are therefore used to study the mechanical residual stress in thin films. The solution that will be discussed involves the biaxial bending of a thin plate [12].

After a film is deposited onto a substrate at an elevated temperature, it cooled to room temperature. When the film/substrate composite is cooled, they contract by different amounts owing to differing coefficients of thermal expansion between the film and the substrate. The film is subsequently strained elastically to match the substrate and remain attached, causing the substrate to bend. This along with the intrinsic film stress developed during film growth, gives rise to a total residual film stress.

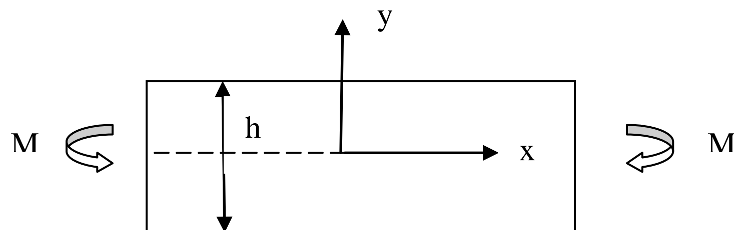

Figure 1.1: Free Body Diagram Showing Bending Moment on a Plate

المنارة للاستشارات
www.manaraa.com

A relationship between the biaxial stress in a plate and the bending moment will now be discussed. Parts of the derivation are based on Nix's analysis [12]. From figure 1 the bending moment per unit length along the edge of the plate M, is related to the stresses in the plate by:

$$M = \int_{-\frac{h}{2}}^{\frac{h}{2}} \sigma_{xx} y dy = y dy = \int_{-\frac{h}{2}}^{\frac{h}{2}} \alpha y^2 dy = \alpha \frac{h^3}{12} \tag{2}$$

Where:

y: is the distance from the neutral axis

α: is a constant and $\sigma_{xx} = \sigma_{zz} = \alpha y$

The stresses are given by:

$$\sigma_{xx} = \sigma_{zz} = \frac{12M}{h^3} y \tag{3}$$

Note that the moment is defined to be positive and will produce a positive stress in the positive y direction. Figure 1.2 below shows a picture of relationship between curvature and strain.

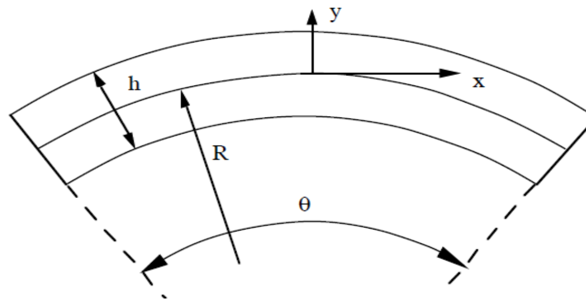

Figure 1.2: Relationship between Bending Strain and Curvature [12]

A negative curvature for pure bending as a result of a tensile strain is shown in figure 1.2.

المنارة للاستشارات
www.manaraa.com

The strain is given by:

$$\in_{xx}(y) = \frac{(R+y)\theta - R\theta}{R\theta} = \frac{y}{R} = -Ky \tag{4}$$

The curvature-strain relationship is thus given by:

$$K = \frac{-1}{R} = \frac{-\in_{xx}(y)}{y} \tag{5}$$

The strain expressed in terms of the biaxial stress is derived from Hooke's law and is given by:

$$\in_{xx} = \frac{(1-v_s)}{E_s}\sigma_{xx} \tag{6}$$

By substitution of equations 3 and 5, the curvature in terms of the biaxial bending moment is given by:

$$K = -\frac{(1-v_s)}{E_s}\frac{12M}{h^3} \tag{7}$$

The results from the bending moment analysis can be extended for both a film and a substrate. It is important to note that the thin film stress equation that will be developed is applicable only for a single thin film on a flat substrate. The film stress equation was first developed by Stoney for a beam [13] but it has since been generalized for a thin film on a substrate. The equation is applicable if the following conditions are satisfied: (1) the elastic properties of the substrate is known for a specific orientation, (2) the thickness of the film is uniform and $t_f << t_s$, (3) the stress in the film is equi-biaxial and the film is in a state of plane stress, (4) the out of plane stress and strains are zero, and (5) the film adhere perfectly to the substrate [14].

المنارة للاستشارات
www.manaraa.com

Figure 1.3 below depicts the force per unit length and the moment per unit length that are acting on the film (F_f and M_f), and substrate (F_s and M_s) respectively. The thickness of the film and the thickness of the substrate are denoted by t_f and t_s.

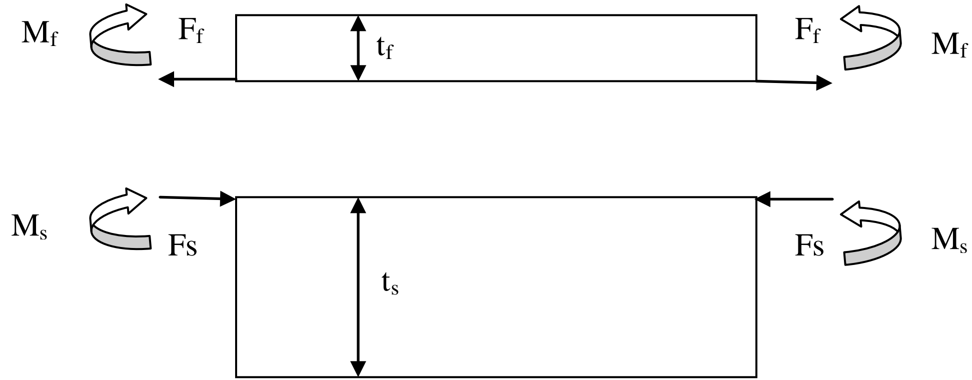

Figure 1.3: Force per Unit Length and Bending Moment per Unit Length Acting on Thin Film and Substrate

If a biaxial tension stress is assumed, then $\sigma_{xx} = \sigma_{zz} = \sigma_f$. The force on the film and substrate are equal and opposite and the film force per unit length is given by: $F_f = \sigma_f t_f$. The moment per unit length of the substrate is thus:

$$M = -\sigma_f t_f \frac{t_s}{2} \tag{8}$$

The resulting curvature of the film/ substrate composite is therefore given by:

$$K = -\frac{(1-v_s)}{E_s}\frac{12M}{h^3} = -\frac{(1-v_s)}{E_s}\frac{12}{{t_s}^3}\left(-\sigma_f t_f \frac{t_s}{2}\right) \tag{9a}$$

$$K = -\frac{(1-v_s)}{E_s}\frac{6\sigma_f t_f}{{t_s}^2} \tag{9b}$$

The stress that a single layer of thin film exerts on a substrate is thus:

$$\sigma_f = \left(\frac{E_s}{1-v_s}\right)\frac{{t_s}^2}{6t_f}k = \left(\frac{E_s}{1-v_s}\right)\frac{{t_s}^2}{6t_f R} \tag{10}$$

المنارة للاستشارات
www.manaraa.com

Where:

E_s is the Young's modulus of the substrate

v_s is the Poisson ratio of the substrate

R is the radius of curvature of the film/substrate composite

Equation (10) is the fundamental equation that calculates the residual stress experienced by a thin film. The equation is applicable for a single film deposited onto a substrate, in which the film thickness is very small compared to the substrate thickness.

1.5 Conclusion and Chapter Objectives

This chapter overviews of the basic parameters and mechanics of solids background to fully understand what contributes to the film stress and more importantly, how it can be minimized. Chapter 2 will discuss the processing of the silicon nitride thin film that includes deposition, measurement of the film thickness, and the residual film stress measurement. Chapter 3 will document and discuss the results that were observed as the flow rates of the PECVD reactant gases and RF plasma power were controlled in order to obtain the low stress film that is desired. In chapter 4, the characterization process will be extended to include how thermal stresses in structures of multiple layers of thin film can be minimized. Finally, chapter 5 will include a discussion on various applications of membrane-based MEMS devices. Particular emphasis will be placed on the design of the MEMS capacitive micromachined ultrasonic transducer.

www.manaraa.com

CHAPTER 2: PROCESSING OF LOW-STRESS SILICON NITRIDE THIN FILMS

2.1 Plasma Enhanced Chemical Vapor Deposition (PECVD) Process

2.1.1 Plasma

Matter exists in four states: solid, liquid, gas, and plasma. Plasma is the most common state of matter and though most of it is not visible, it comprises about 99% of our visible universe [15]. Plasma occurs naturally and exists on the earth in flames, lightening, and the auroras; plasma is even a part of our sun, the core of stars, x-ray beam emitting pulsars, and supernovas. The plasma gas carries an electrical charge. The gas is comprised of approximately the same number of positively charged ions and electrons. Plasma is therefore a mixture of neutrally ionized gas which allows positively charged ions and electrons to coexist, when enough energy is supplied to the gas to free electrons from atoms or molecules. Because plasma contains a large amount of positive ions with very high kinetic energy, it plays a very important role in micro-fabrication. In micro-fabrication, plasma can be used to [2]: deposit films onto a substrate material, and to remove a portion of base material by knocking out the atoms from that material. In this research, plasma is used to assist in depositing silicon nitride thin film to a silicon substrate in a process known as Plasma Enhanced Chemical Vapor Deposition (PECVD).

المنارة للاستشارات
www.manaraa.com

2.1.2 Chemical Vapor Deposition (CVD)

In micromachining, there are essentially two classes of deposition: Physical Vapor Deposition (PVD) and Chemical Vapor Deposition (CVD) [2]. In Physical Vapor Deposition, particles are directly impinged on a hot substrate. An example of physical vapor deposition is sputtering, which is used to deposit thin metallic films onto the surface of a substrate material. In CVD, source gases are first introduced into a reaction chamber. Energy is then supplied to these gases in the form of either heat, plasma generation, or other techniques. The energy created cause a chemical reaction, which results in the decomposition of the source gas and reaction of chemicals to form a solid film. The by-products of the chemical reaction can then be vented. Examples of Chemical Vapor Deposition are: Plasma Enhanced CVD, Low Pressure CVD, and Atmospheric Pressure CVD.

2.1.3 Plasma Enhanced Chemical Vapor Deposition (PECVD)

An advantage of employing plasma is the relative ease of altering the flow rate by using electrostatic forces of magnetic fields [2]. PECVD uses RF plasma to transfer energy into the reactant gases in a reaction chamber, and the chemical reaction will not occur without the creation of plasma.

The PECVD reactor used in this project was manufactured by Uniaxis USA, Inc (St. Petersburg, FL) and is shown in figure 2.1. The reactor uses electromagnetic radiation and has RF frequency in two modes: low frequency (50 kHz) and high frequency mode (13.56 MHz). The use of an RF source to create the plasma in Plasma Enhanced CVD significantly reduces the deposition temperature unlike in the case of

المنارة للاستشارات
www.manaraa.com

Atmospheric Pressure CVD and Low Pressure CVD which can have deposition temperatures of up to 900^0C. This high temperature may cause a measurable damage to the substrate material and other undesirable effects that can alter the device performance. The first commercial application of Plasma Enhanced CVD was the low temperature deposition of silicon nitride at 300^0C. A view of the PECVD system used in this project is shown in figure 2.1.

Figure 2.1: Plasma Enhanced Chemical Vapor Deposition (PECVD) System Used to Deposit and Characterize Silicon Nitride Thin Film

المنارة للاستشارات
www.manaraa.com

In this project, a low temperature Plasma Enhanced CVD process was used to deposit silicon nitride with a deposition temperature of only 250^0C at a vacuum pressure of 900 mTorr. The stress in the silicon nitride thin film was controlled by changing the silane or nitrogen gas flow rates, and the RF plasma power in high frequency mode.

2.2 Wafer Preparation and Silicon Nitride Deposition

The substrate used for the characterization of the silicon nitride thin films were all 50 mm (2 inch) <100> crystallographic orientation, n-type bare silicon wafers with resistivity 0.4-0.6 Ω cm. The wafers were first cleaned by dipping in Hydrofluoric acid (HF) for 2 minutes, followed by rinsing with D.I water. A standard solvent clean was then performed using methanol, acetone, and D.I water. The wafers were then dried individually with nitrogen gas.

The deposition was carried out using a Plasma-Therm 700 PECVD system (Uniaxis USA, Inc). In this system the plasma can be activated in either a low frequency mode LF (50 KHz), or a high frequency mode HF (13.56 MHz). In this experiment, a high frequency mode was used, as is typical for this type of characterization [11], [16]. Silicon nitride films were deposited using reactant gases of pure silane (SiH_4) and nitrogen (N_2) for which the flow rate could be changed. The RF plasma power was also adjustable. Literature has shown that high-quality film can be obtained by keeping the deposition temperature and the vacuum pressure within the reactor constant [8], [10-11], [16]. In addition, better quality film can be obtained if the vacuum pressure is substantially small, for example in the range of 900-1200 mTorr [16]. In one experiment,

المنارة للاستشارات
www.manaraa.com

detail analysis of PECVD silicon nitride revealed that a pressure of around 900 mTorr is optimal for silicon nitride deposition due to its stable plasma and low- residual stress generated [11]. In this project, a constant deposition temperature of 250^{0}C and a vacuum pressure of 900 mTorr were used for all the characterization. In addition, all samples to be deposited with silicon nitride were processed separately based on its PECVD recipe.

2.3 Silicon Nitride Film Thickness Measurement

The thickness of the silicon nitride film was measured optically using a Rudolph Ellipsometer Auto EL3 (Rudolph Instruments, Denville NJ). This instrument was chosen due to its accuracy in measuring highly transparent film on a reflective surface that has thicknesses in the order of 10Å to 3µm [17]. In addition, the index of refraction of PECVD silicon nitride varies based on the fabrication process parameters. The ellipsometer allows the measurement of the index of refraction. The system uses a helium-neon laser as the optical light source with an operating wavelength of 632.8 nm. The method of ellipsometry used to determine the properties of films on a silicon substrate has been studied by a number of researchers [18-19]. In summary, the ellipsometer measure the changes in the state of polarization of collimated beams of monochromatic polarized light caused by reflection from the surfaces of a substrate. Using an electric field representation, the incident and reflected beam can each be resolved into two perpendicular linearly-polarized components p and s. The p component has its electric field vector parallel to the plane of incidence while the s component will have its vector normal to the plane of incidence [20]. Whenever a collimated beam of

المنارة للاستشارات
www.manaraa.com

monochromatic polarized light is reflected from any surface, this causes a phase difference and a change in the relative amplitudes of the p and s components. From these changes, two angles delta and psi can be determined and be transformed into measurements of thickness and refractive index [17], [20].

In this thesis, the ellipsometer was used to measure the thickness of a single layer of silicon nitride and the index of refraction. A customized five point measuring scheme was used in which measurements were taken at the center of the substrate and then along four corners. The averages of these measurements were taken which improve the overall result accuracy. In addition, the film thickness measurement obtained by the ellipsometer was verified by etching one sample and measuring the step height using a profilometer. The measurements were found to be in close agreement. This etched sample is used as a reference to verify the accuracy of the ellipsometer before recording the film thickness of a newly deposited nitride sample. A picture of the ellipsometer used for the film thickness measurements is shown in figure 2.2.

المنارة للاستشارات
www.manaraa.com

Figure 2.2: Ellipsometer Used to Measure the Thickness of the Silicon Nitride Film

2.4 Residual Film Stress Measurement

Silicon nitride thin films deposited using PECVD usually develops some internal or residual stress. In this experiment, the stress of the nitride film was determined using the wafer curvature technique. A Veeco Dektak 150 Surface Profilometer (Veeco Instruments Inc, Woodbury New York) shown in figures 2.3 and 2.4 was used to measure the radius of curvature before and after the film deposition. It is important to note that the

المنارة للاستشارات
www.manaraa.com

orientation of the wafer was kept unchanged throughout the measurement of the film stress on each wafer. Three stops were used to keep the wafer in place (figure 2.4) which promotes consistency and accuracy in the results that are obtained. The radius of curvature is an important parameter used to compute the film stress [21]. Using this method, the height of the substrate can be modeled as a continuous function of distance along the substrate, y= $f(x)$. The radius of curvature can then be calculated using:

$$R(x) = \frac{(1+y'^{2})^{\frac{3}{2}}}{y''} \tag{11}$$

Where:

$y' = \frac{dy}{dx}$, and $y'' = \frac{dy^2}{dx^2}$

المنارة للاستشارات
www.manaraa.com

Figure 2.3: Surface Profilometer Used to Measure the Curvature in the Silicon Substrate and Compute the Film Stress

المنارة للاستشارات
www.manaraa.com

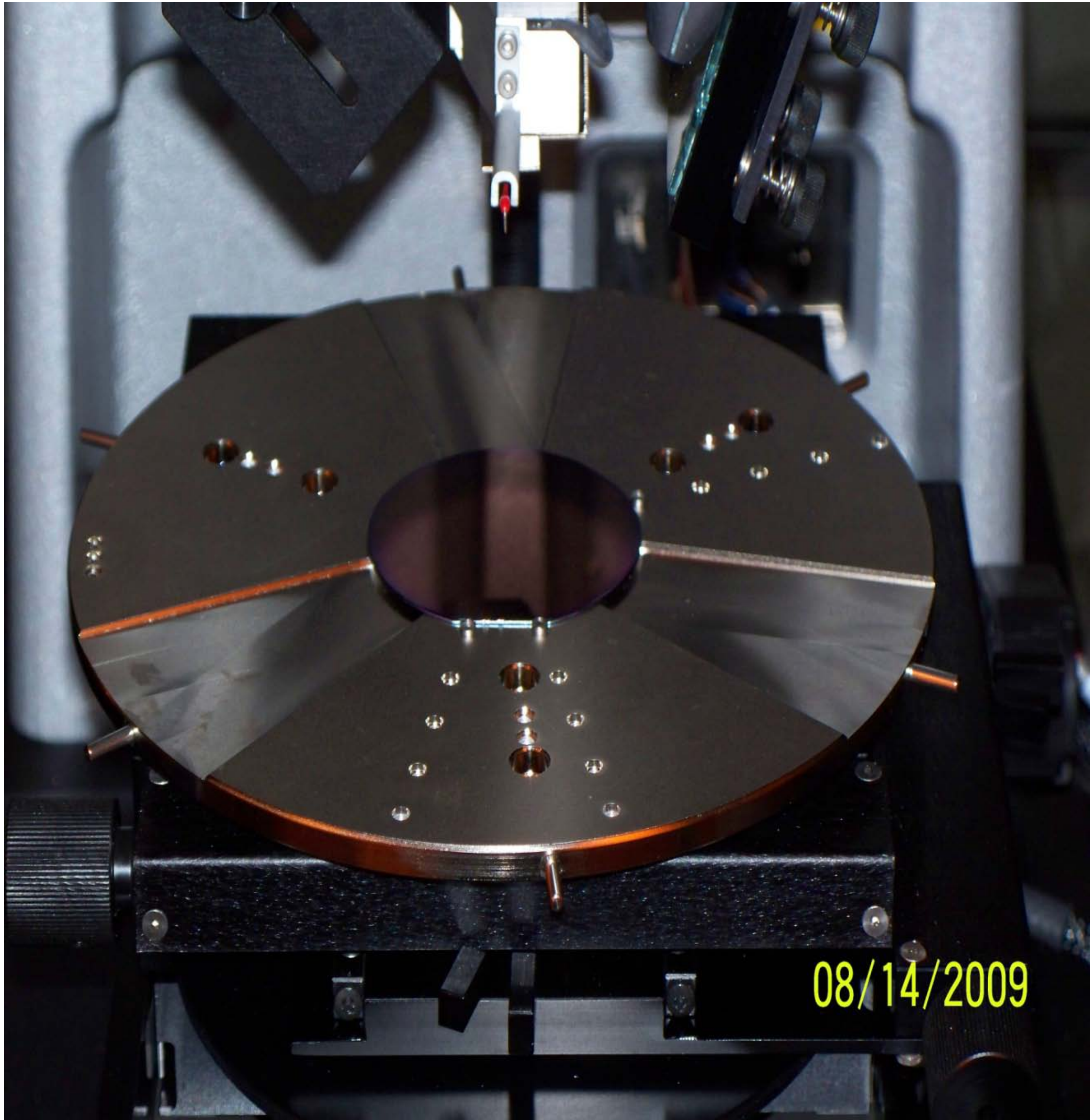

Figure 2.4: Silicon Wafer Mounted on the Surface Profilometer with Three Stops Used to Restrict Movement of the Wafer

A scan of the substrate is taken prior to deposition, and after depositing the silicon nitride film. Each scan is fitted with a fifth order polynomial by the method of least squares. The fit is differentiated to obtain y' and y'' as noted above, which are substituted in equation (11) that gives the radius of curvature before the deposition and

المنارة للاستشارات
www.manaraa.com

after the deposition as a function of scan position. A pre-deposition scan of one of the samples used in this experiment is shown in figure 2.4 below.

Figure 2.5: Scan of a Wafer before Deposition of Silicon Nitride

By measuring the thickness of the film, and entering known parameters for the substrate, the stress of the silicon nitride thin film is calculated using [22]:

$$\sigma_f = \frac{1}{6}\left[\frac{1}{R_{postdep}} - \frac{1}{R_{predep}}\right]\frac{E}{(1-v_s)}\frac{{t_s}^2}{t_f} \qquad (12)$$

Where:

المنارة للاستشارات
www.manaraa.com

σ_f = stress in silicon nitride film after deposition

R_{predep} = substrate radius of curvature before deposition

$R_{postdep}$ = substrate radius of curvature after deposition

E = Young's Modulus of the silicon substrate

v_s = Poisson's ratio of the silicon substrate

t_s = thickness of the substrate

t_f = thickness of the silicon nitride film

The pre-deposition and post-deposition curvatures are determined, and equation (12) is used to calculate the residual stress of the silicon nitride film. Negative values indicate a compressive stress for a convex surface while positive values indicate a tensile stress for a concave surface. The units for the measured stress are Dynes per square centimeters (1 Dyne = 10^{-5} Newton) [22]. The accuracy of the measured stress is improved by increasing the scan length around the center of the substrate (typically 70% or more) and using a large diameter stylus [22]. In this experiment, a 40 mm scan length (80% of the 50 mm substrate) and a 12.5µm radius stylus were chosen from stylus of radii 2.5 µm, 5 µm, and 12.5 µm, to allow for higher speed scanning without scratching. For the 40 mm scan length, two sets of results were obtained for the computed stress. The stress values were first computed between a 15 mm to 25 mm area around the center of the substrate, and then between a 5 mm to 35 mm area around the substrate's center. This was done for comparison and to show that even though a scan is taken across a 40 mm length, there is some flexibility in calculating the stress. The final stress value for a sample was calculated by computing the average of the stress values obtained for the 15

المنارة للاستشارات
www.manaraa.com

mm to 25 mm scan area (figure 2.5), and the 5 mm to 35 mm scan area (figure 2.6). Figure 2.7 show an example of the result that is obtained from scanning the substrate and computing the film stress.

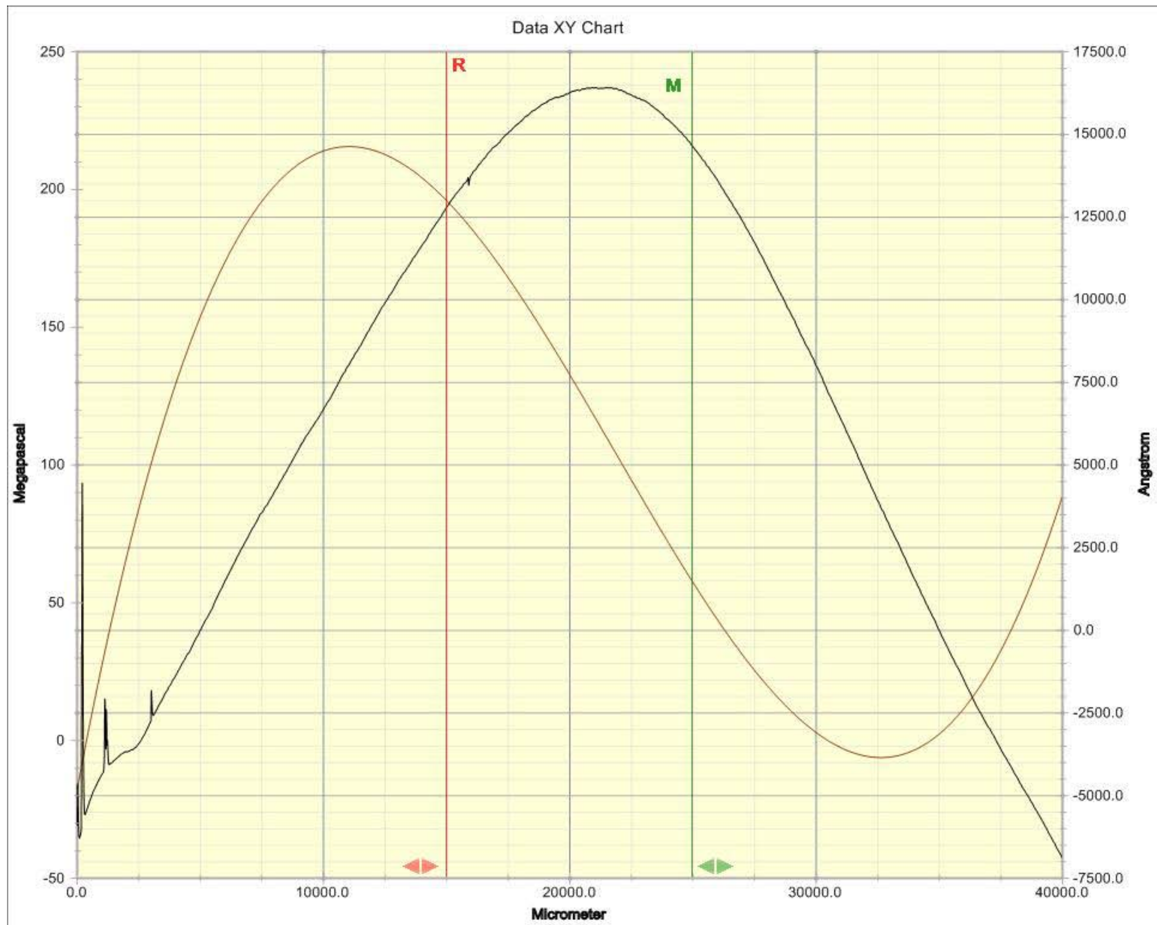

Figure 2.6: Post-deposition Scan of Silicon Wafer with Silicon Nitride Film and Stress Computed between 15 mm and 25 mm on the Surface of the Wafer

المنارة للاستشارات
www.manaraa.com

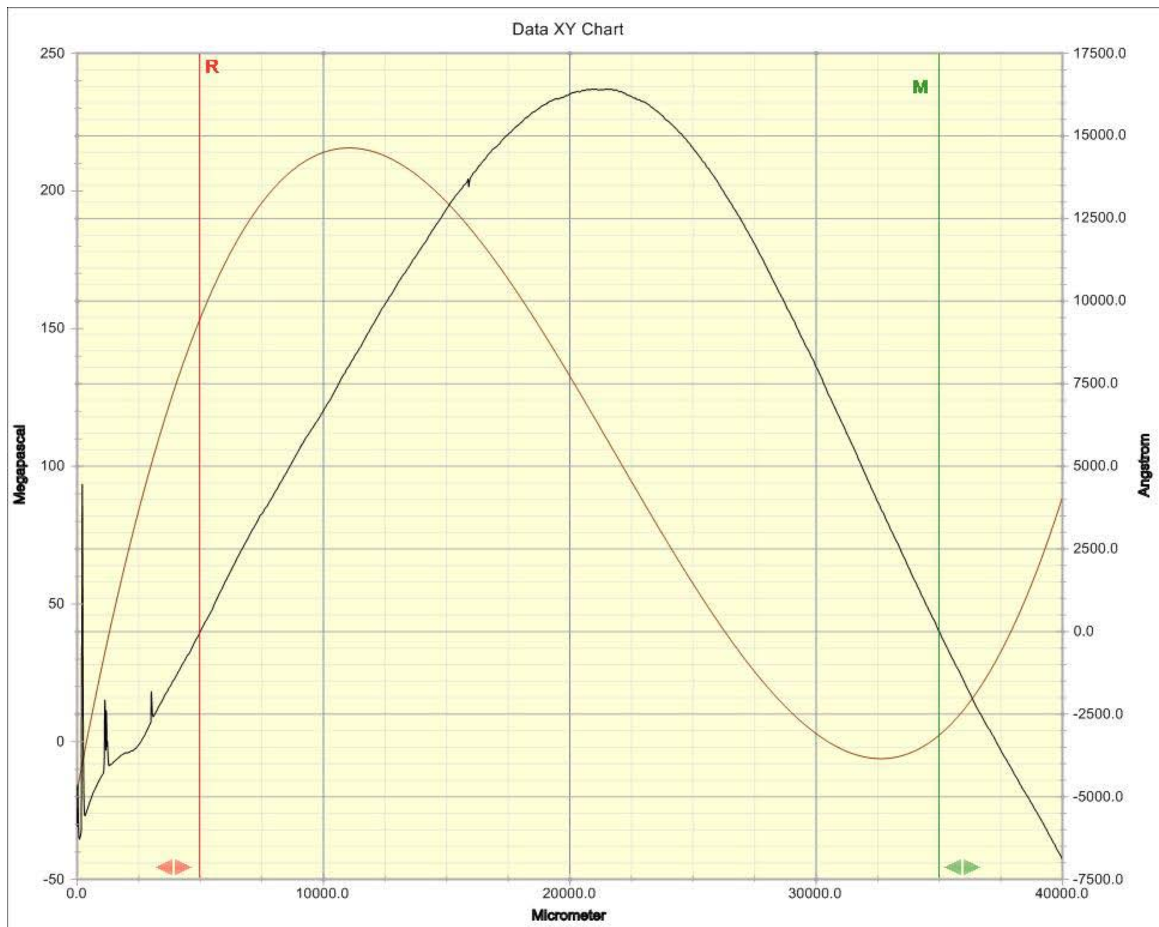

Figure 2.7: Post-deposition Scan of Silicon Wafer with Silicon Nitride Film and Stress Computed between 5 mm and 35 mm on the Surface of the Wafer

www.manaraa.com

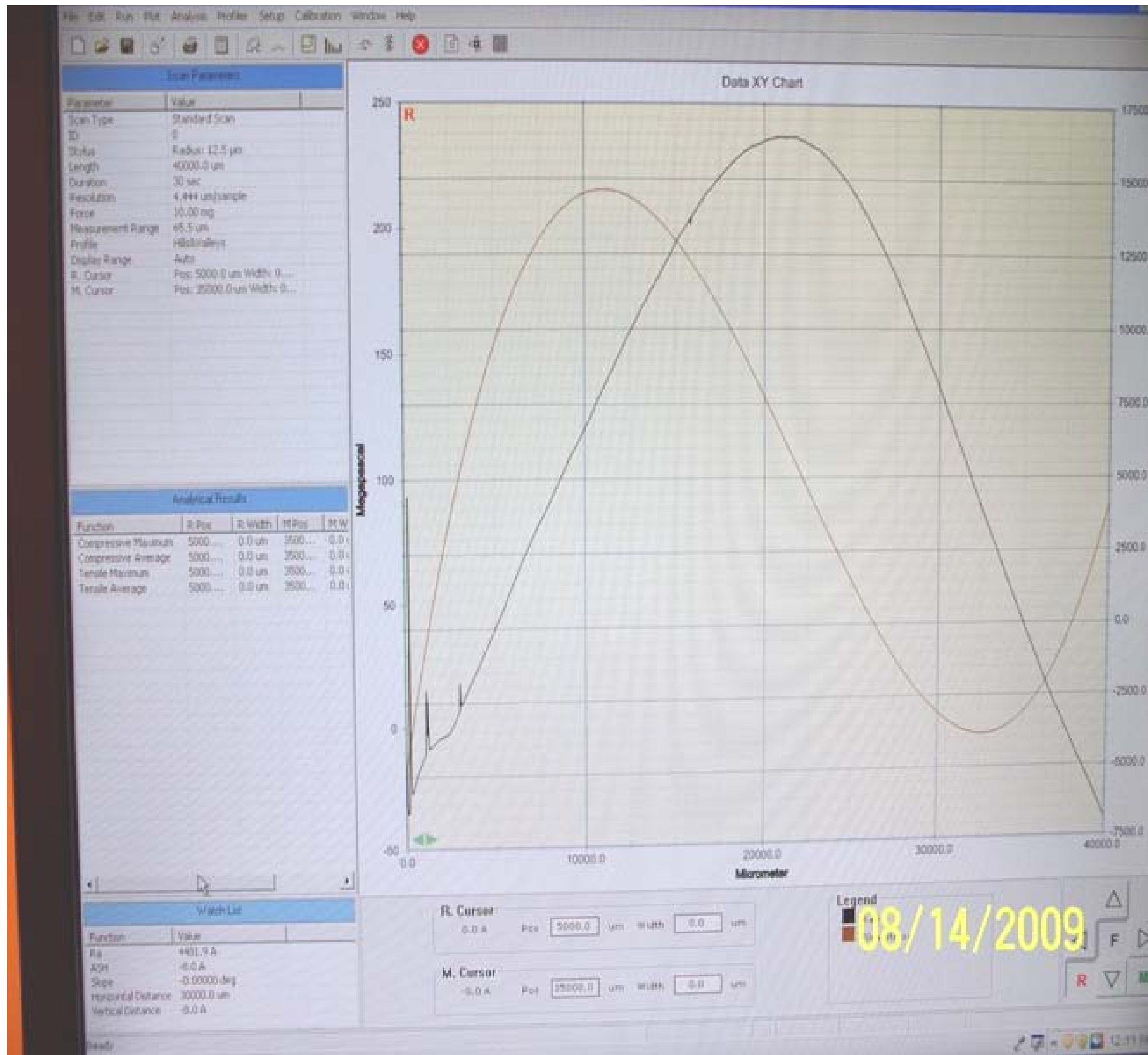

Figure 2.8: An Example of the Output Obtained From Scanning the Wafer before and after Deposition of Silicon Nitride and Computing the Residual Stress

The measured stress is the residual film stress that a single layer of film exerts on a silicon substrate. As stated before, and in equation (1), the residual film stress σ_r, is the summation of the thermally induced stress $\sigma_{t,}$ in the silicon substrate/film arrangement and the intrinsic film stress, σ_i [12], [23]. The thermal stress is due to the film and the substrate having a different coefficient of thermal expansion. Because of this, when the film and substrate is exposed to a certain temperature (as in the PECVD chamber) and

المنارة للاستشارات
www.manaraa.com

then allowed to cool, they expand/contract by different amounts. The film is therefore strained as it becomes attached to the substrate, resulting in thermal stress. Intrinsic film stress is the stress developed from processes such as nucleation and growth and phase transformation as the film is being grown.

2.5 Accuracy of Method Used to Determine Film Stress

Equation (12) is the basic equation that is used to calculate the residual film stress. One can observe from this equation that the only parameter measured by the Dektak surface profiler is the radius of curvature. This of course, is done by taking a scan of the substrate before and after deposition. This equation is an extension of the original equation presented by Stoney [14] in 1909 that is used to calculate the film stress on an isotropic substrate. The original expression developed by Stoney reads:

$$\sigma = \frac{1}{6}\frac{E}{R}\frac{{t_s}^2}{t_f} \qquad (13)$$

Where:

R= radius of curvature of the substrate after deposition

In the above equation, an initially flat substrate was assumed. Equation (13) has since been modified and was first presented in 1987 in the form of equation (12) by Nix et al. [24]. The new factor 1/ $(1 - v_s$) in equation (12) has been introduced because one of the assumption in using the originally developed Stoney equation is that the width of the film is much larger than its thickness, hence the film stress is bi-axial [14]. In summary, use of equation (12) requires that: (1) the elastic properties of the substrate are known for a specific orientation, (2) the thickness of the film is uniform and $t_f << t_s$, (3)

المنارة للاستشارات
www.manaraa.com

the stress in the film is bi-axial and the film is in a state of plane stress (the plane of the film stress is independent of direction), (4) the substrate is thin, and (5) the film adhere perfectly to the substrate [14]. Equation (12) was used for our analysis as the above requirments have been met. The orientation and elastic properties of the substrate were known, and these were used as inputs to the surface profilometer before each scan was taken. The standard deviation for each 5 point thickness measurement was relatively small when measured by the ellipsometer. The average thickness of the films was about 100 nm compared to a typical 550 μm substrate thickness.

المنارة للاستشارات
www.manaraa.com

CHAPTER 3: SILICON NITRIDE FILM CHARACTERIZATION

3.1 Overview of Data Collected

In all the test data, the flow rate of the pure silane gas (SiH_4), the vacuum pressure, and the deposition temperature remained constant. Two main parameters were changed throughout the experiment namely: the flow rate of the nitrogen gas (N_2), and the RF power. In the experiment, the flow rate of the SiH_4 gas was kept constant as this was sufficient to provide enough data for the stress analysis. The main parameters that were used to assess the quality of the silicon nitride film are film stress, refractive index, and etch rate. There is a strong correlation between the stoichiometry of silicon nitride film and the refractive index. This correlation has shown that the refractive index can be used as a measure to determine the quality of the deposited film. Stoichiometric silicon nitride thin films are almost inert to most common wet etchants, and a higher refractive index usually means higher etch selectivity [25]. The acceptable values for the index of refraction of PECVD silicon nitride is 1.8- 2.5 [3]. The importance of the etch rate is that higher etch rate is indicative of more pinhole defects and air in the film as a result of increased porosity. A lower etch rate therefore, usually indicate a better quality film.

المنارة للاستشارات
www.manaraa.com

3.2 Effect of RF Power

The first experiment began with a RF power of 50 W. The original recipe for the characterization is summarized in table 3.1 below.

Table 3.1: Original PECVD Silicon Nitride Recipe

Parameter	**Sample 4**
Pure Silane (SiH_4)	5 sccm
N_2	1000 sccm
Pressure	900 mTorr
Power	50 W
Temperature	250 ^{0}C
Time	10 min

Our results indicate that the average film thickness measurement using the Rudolph Ellipsometer was determined to be 1240 ± 16.4 Å. The corresponding index of refraction was measured to be 2.352 ± 0.009. Using these values, the post deposition stress was measured using the Veeco Dektak 150 profilometer indicating average silicon nitride film stress as 61.3 ± 5.9 MPa (tensile).

To investigate the effect of RF power on the stress, the RF power was first increased from 50 W to 60 W while keeping the other parameters constant. We could not obtain a measurement of the film thickness at this RF power value. This result showed that increasing the RF power beyond a certain point while keeping the other parameters the same can significantly increase the thickness non-uniformity of the film.

المنارة للاستشارات
www.manaraa.com

Next, we reduced the RF power to 45 W. Table 3.2 summarize the recipe used in this portion of the characterization process.

Table 3.2: Modified PECVD Silicon Nitride Recipe with RF Power at 45 W

Parameter	**Sample 5**
Pure Silane (SiH4)	5 sccm
N_2	1000 sccm
Pressure	900 mTorr
Power	**45 W**
Temperature	250 ^{0}C
Time	10 min

From the PECVD recipe in table 3.2, the important measurements that were collected are the thickness of the film and the refractive index, as measured by the ellipsometer. These values were found to be 1143 ± 6.1 Å, and 2.480 ± 0.012 respectively. Using the measured film thickness value, the stress was determined on the Dektak profilometer to be 11.3 ± 5.3 MPa. In comparing the results from the recipe in table 3.1 and table 3.2, a number of inferences can be made. The first is that there were hardly any differences between the thicknesses in the film that were deposited at a power of 50 W and at a power of 45 W. The second observation was that the measured stress at 45 W had reduced substantially when compared to the stress measurement taken at 50 W. This lower average stress value at a RF power of 45 W is due to the fact there is more of

www.manaraa.com

a even distribution between the negative compressive stress and the positive tensile stress in the film. When the average film stress is computed across a scan range, the tensile stress dominates.

The effect of reducing the RF power was compared to previous work done by [10] in which reducing RF power had resulted in an increase in residual stress. The PECVD system used in this work however is different and some other parameters were not the same. For example, no ammonia gas was used in our experiment and the RF power used in [10] was varied between 75 W to 125 W. This result has shown that data obtained can vary in different PECVD equipment. Most of the results that will be discussed from here on however, have been shown to be in close agreement to that obtain in the literature.

We have discussed that the index of refraction of the silicon nitride film can be a measure of the quality of the film. When the RF power was reduced to 45 W with all other parameters remaining constant, the refractive index of the film increased from 2.35 to about 2.48. This increase has indicated that the quality of the film might have been improved; in that, a higher index of refraction has defined higher etch rate resistance [8]. It is also interesting to note that at a higher RF power, the deposition rate tends to increase. This is because a higher power enhances the plasma in the deposition chamber which increases the energy of electrons which results in an increased dissociation of the main gases [11].

المنارة للاستشارات
www.manaraa.com

3.3 Effect of Deposition Time

The recipes in table 3.1 and table 3.2 were repeated with two separate samples and the deposition time was reduced to 7 minutes in an attempt to achieve film thickness at around 1000 Å. Based on the results obtained, there was no clear correlation between the deposition time and the measured stress in the silicon nitride film. The recipes of the two samples are summarized in table 3.3.

Following the deposition of the silicon nitride layer onto both samples, the values obtained from the ellipsometer for sample 1 had thickness and index of refraction measurements of 911 ± 3.5 Å and 2.513 ± 0.003 respectively. The thickness of this sample at a deposition time of 7 minutes was lower than the value obtained for the 10 minute run and closer to the 1000 Å target. The index of refraction had increased from the previous result of 2.352 obtained with a deposition time of 10 minutes.

Table 3.3: PECVD Recipe with Modified Deposition Time

Parameter	**Sample 1**	**Sample 2**
Pure Silane (SiH_4)	5 sccm	5 sccm
N_2	1000 sccm	1000 sccm
Pressure	900 mTorr	900 mTorr
Power	**50 W**	**45 W**
Temperature	250 ^{0}C	250 ^{0}C
Time	**7 min**	**7 min**

المنارة للاستشارات
www.manaraa.com

Similar results were observed in sample 2 which had film thickness and refractive index measurements of 886 ± 3.4 Å and 2.567 ± 0.004. The measured stress in sample 2 was mostly tensile with a value of 18.5 ± 1.41 MPa while the tensile stress in sample 1 was 37.25 ± 3.89 MPa. The results are summarized in table 3.4. The most important result in this section is that regardless of deposition time, a reduction in the RF plasma power has resulted in both a lower stress film and increased index of refraction. It can be concluded therefore that reducing the RF plasma power and keeping certain parameters constant can give rise to better quality silicon nitride films.

Table 3.4: Results Obtained when the Deposition Time was Changed to 7 Minutes

	Sample 1	Sample 2
RF Power (W)	50	45
Film Thickness (Å)	911 ± 3.5	886 ± 3.4
Film Stress (MPa)	37.25 ± 3.89	18.5 ± 1.41
Index of Refraction	2.513 ± 0.003	2.567 ± 0.004

3.4 Effect of Nitrogen Flow Rate

In a second experiment, the original recipe as outlined in table 3.1 was taken but the nitrogen gas (N_2) flow rate was reduced from 1000 sccm to 800 sccm. It is important to realize that N_2 is responsible for supplying the N atoms for the reaction. Decreasing the N_2 flow rate should lead to a 'Si-rich' silicon nitride layer which has a lower residual stress [11].

المنارة للاستشارات
www.manaraa.com

Table 3.5: Comparison of Original Recipe and the Effect of Reduced N_2

Parameter	**Original recipe**	**New sample**
N2	1000 sccm	800 sccm
Thickness	1240 ± 16.4 Å	1314 ± 77.3 Å
Index of refraction	2.352 ± 0.009	2.751 ± 0.135
Stress (MPa)	61.35 ± 5.87	42.75 ± 13.08
Time	10 min	10 min

From table 3.5, the residual film stress is reduced by lowering the nitrogen gas flow rate while keeping the other parameters constant. The thickness of the film was in the same range as compared to the original recipe. It was also observed that the index of refraction had increased, indicating that a better etch rate is expected. The downside of using a lower nitrogen gas flow rate however, is the increased non-uniformity in the film thickness.

By using the original recipe with 60 W RF power, a thickness measurement could not be determined. Hence the recipe was modified as shown below.

المنارة للاستشارات
www.manaraa.com

Table 3.6: Increasing RF Power with Reduced N_2 Flow Rate

Parameter	**Original recipe**	**Modified recipe**
Pure Silane (SiH4)	5 sccm	5 sccm
N2	**1000 sccm**	**800 sccm**
Pressure	900 mTorr	900 mTorr
Power	**50 W**	**60 W**
Temperature	250 ^{0}C	250 ^{0}C
Time	10 min	10 min

In the modified recipe, a nitrogen gas flow rate of 800 sccm was used. As we have concluded before (table 3.5), it is possible to obtain a better quality film with lower residual stress with lower nitrogen gas flow rate. With this modified recipe, the results were as follows: the film thickness measurement was determined to be 1698 ± 21.9 Å, the index of refraction was 2.266 ± 0.023, and the residual film stress was determined to be 91.75 ± 0.35 MPa. The results have shown that an increase in RF plasma power beyond a certain point can reduce the quality of film. This is shown by an increased in residual film stress and a decrease in the index of refraction which negatively impacts the film quality.

To further study the effect of a reduced nitrogen gas flow rate on the film stress, an additional recipe was developed which was slightly modified from that of sample 2 in table 3.3. The PECVD recipe of sample 2 is presented in table 3.7 along with the recipe for the sample to be analyzed.

المنارة للاستشارات
www.manaraa.com

Table 3.7: Effect of a Reduced N_2 Flow Rate with Reduced Power and Time

Parameter	**Sample 2**	**Adjusted recipe**
Pure Silane (SiH4)	5 sccm	5 sccm
N2	**1000 sccm**	**900 sccm**
Pressure	900 mTorr	900 mTorr
Power	**45 W**	**45 W**
Temperature	250 ^{0}C	250 ^{0}C
Time	7 min	7 min

Using the modified recipe above, the thickness of the deposited silicon nitride film was 950 ± 2.4 Å, similar to that of sample 2. The measured refractive index was 2.663 ± 0.009, increased from 2.567 as compared to sample 2. We found that the residual film stress obtained using this recipe was compressive. At some measurement points however, the residual stress was tensile making the average residual stress very low tensile (1.25 ± 30.05 MPa). This result has shown that by using optimized parameters for the PECVD, high quality silicon nitride thin film with very low stress can be obtained.

The important conclusion from the PECVD silicon nitride films characterization experiments are as follows. 1) RF power directly affects the quality of the silicon nitride films. Low stress film is obtained by using low RF power with optimized silane and nitrogen gas flow rates. 2) A lower N_2 gas flow rate is desired to achieve low stress PECVD silicon nitride. Also, a higher SiH_4 to N_2 gas flow rate ratio gives lower overall film stress values.

المنارة للاستشارات
www.manaraa.com

3.5 Effect of Pressure

The lower vacuum pressure directly influences the stability of the generated plasma [26]. Previous experiments indicate that a pressure around 900 mTorr is ideal for low residual stress characterization with stable RF plasma power [11], [26-27].

3.6 Plasma Etch: Overview of Process

A portion of the silicon nitride film was etched on each of three substrates that were deposited with silicon nitride. This was done in the plasma dry etch chamber that was configured to the PECVD system. A separate method was used to determine the thickness of the film after etching. This method utilizes a step-height technique which is more appropriate for measuring film thickness. A special captone tape (figure 3.1) was used to protect a part of the film from etching. An Alpha-Step Profilomer (Tencor instruments, Mountain View California) was then used to measure the step. The step-height is determined by comparing the thickness of the etched portion of the film to the un-etched portion.

Table 3.8: Recipe for Plasma Etch

CF_4	80 sccm
O_2	4 sccm
Pressure	250mTorr
RF Power	100 W
Time	20-30 secs

المنارة للاستشارات
www.manaraa.com

Table 3.8 gives a summary of the plasma etch recipe used to characterize the etch rate of the silicon nitride layer. Table 3.9 presents the samples that were used for etching based on their PECVD silicon nitride recipe along with the film thickness, index of refraction and the measured residual film stress.

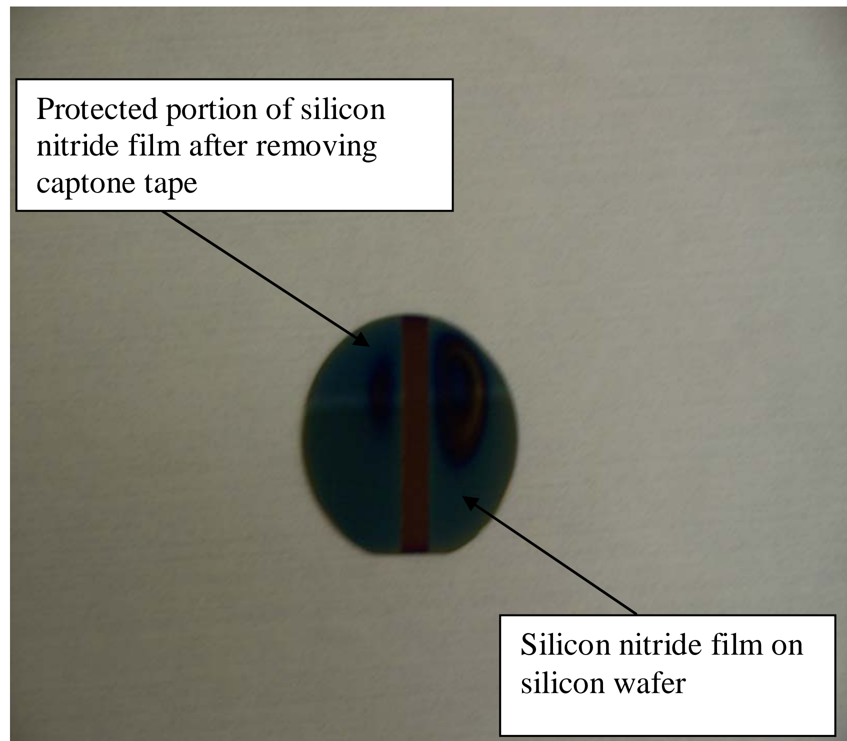

Figure 3.1: Silicon Nitride Film on a Wafer with Region that was Protected with Captone Tape Clearly Visible after Plasma Etch

المنارة للاستشارات
www.manaraa.com

Table 3.9: Samples Used for Plasma Etch

Parameter	Sample A	Sample B	Sample C
Pure Silane (SiH_4)	5 sccm	5 sccm	5 sccm
N_2	**1000 sccm**	**1000 sccm**	**800 sccm**
Pressure	900 mTorr	900 mTorr	900 mTorr
Power	**50 W**	**45 W**	**50 W**
Temperature	250 ^{0}C	250 ^{0}C	250 ^{0}C
Time	10 min	10 min	10 min
Thickness	1249 ± 47.6 Å	1016 ± 15.7 Å	1305 ± 133 Å
Refractive Index	2.563 ± 0.074	2.911 ± 0.031	2.69 ± 0.263
Stress (MPa)	**24.75**	**3.25**	**16.25**

From the results above, it can be seen that the thickness, Refractive index, and stress values agrees reasonably well to those samples that were previously characterized. The stress values were lower in table 3.9 than those of the first samples that were analyzed. However, it is found out that the general trend is similar.

3.7 Etch Rate Comparison

As previously discussed, the refractive index can be used as a measure of the quality of the film in terms of etch rate. Hence, we expect the film with the highest refractive index to have a lower etch rate compared to the other films. The step height of the three samples was measured individually with an Alphastep Profilometer (figure 3.2).

المنارة للاستشارات
www.manaraa.com

The samples were etched using a plasma dry etch tool and the etch time for samples A, B, and C, were 25, 20, and 20 seconds respectively. The resulting etch rates were calculated and are summarized in table 3.10. It should be seen that the sample with the largest index of refraction (Sample B) had a lower etch rate as expected, when compared with the other samples which agrees with what was expected.

Table 3.10: Summary of Etch Rates

Parameter	**Sample A**	**Sample B**	**Sample C**
Height (Å)	750	500	600
Time (s)	25	20	20
Etch Rate (Å/s)	30	25	30

www.manaraa.com

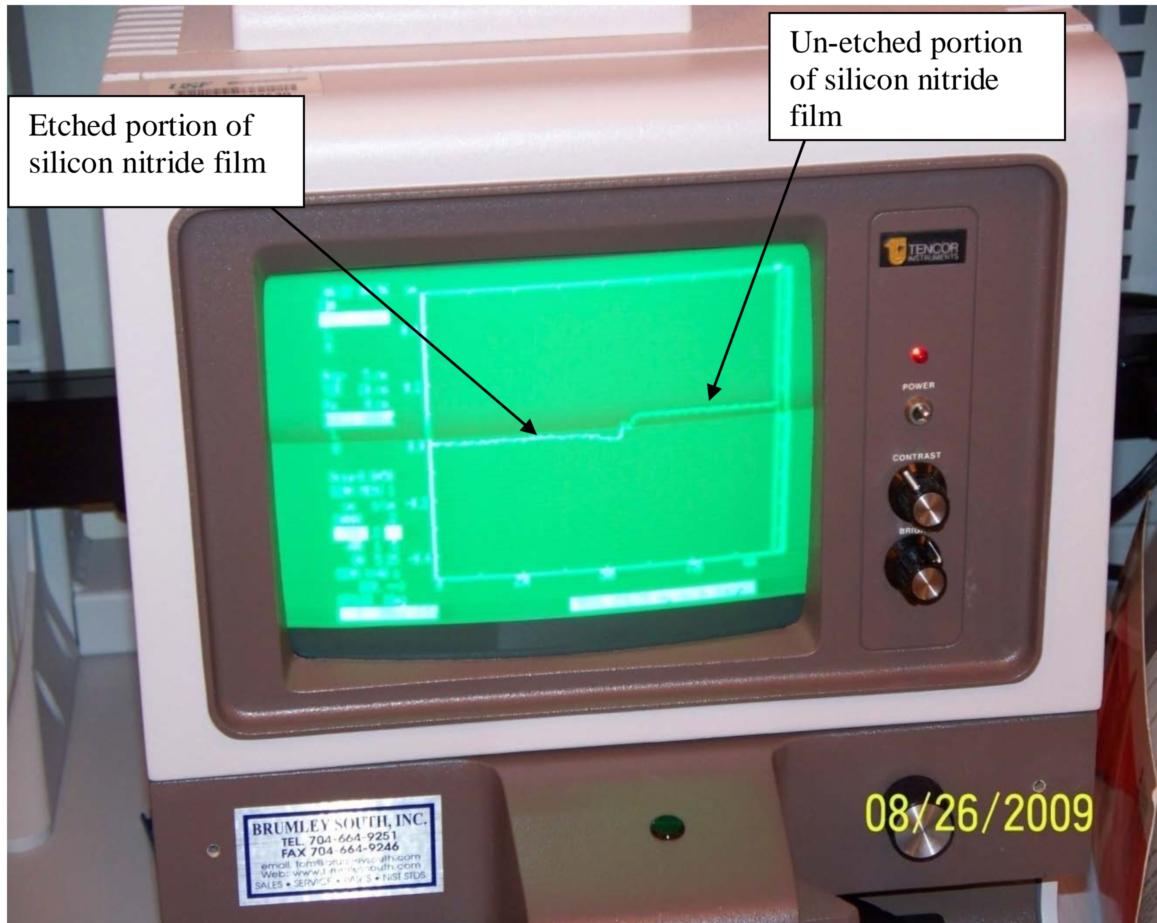

Figure 3.2: Alpha-Step Profilometer Used to Measure Silicon Nitride Step Height From One Surface of the Etched Portion of the Nitride Film to the Un-etched Portion

المنارة للاستشارات
www.manaraa.com

CHAPTER 4: THERMAL STRESS EFFECTS IN MULTI-LAYER MEMS STRUCTURES

4.1 Overview of Thermal Stress in Thin Films

The residual film stress is the stress that is present in a thin film after a deposition process. This overall stress has two components: the thermal mismatch stress, and the intrinsic stress. The thermal mismatch stress is due to the film and substrate having different thermal expansion coefficients while the intrinsic film stress is composed of parameters induced during nucleation and growth [1], [28]. Intrinsic stress might include stress contributions from: (1) recrystallization processes, (2) incorporation of atoms (residual gases), (3) differences in lattice spacing of monocrystaline substrates and the film during epitaxial growth, (4) microscopic voids and special arrangements of dislocations, (5) phase transformation, and (6) variation of the interatomic spacing with the crystal size [29-30].

In this chapter, the thermal stress effects on multi-layer systems will be discussed and analyzed. This analysis is directly applicable to MEMS devices as they are composed of multiple layers of patterned thin films. The effects of the thermal stress becomes apparent in multi-layer systems when the system bends as a result of each layer of thin film having different thermal expansion coefficients.

المنارة للاستشارات
www.manaraa.com

In many applications, particularly in the area of optical MEMS, flat thin films surfaces are necessary for optimal performance [31]. Highly stressed layers of thin films may affect the proper functioning of a device.

4.2 Background Equations on Thermal Stress in Thin Films

The equations in this section were developed for thin films that are deposited onto a stress-free layer at temperature T_d and allowed to cool to room temperature, T_r. It is assumed that the deposited thin film will contract by the same amount as the substrate [1]. The thermal strain on a substrate (in one in-plane dimension) is given by:

$$\epsilon_s = -\alpha_{Ts} \Delta T \tag{14}$$

Where:

α_{Ts} is the linear thermal expansion coefficient of the substrate and, $\Delta T = T_d - T_r$

The thermal strain for a thin film that is not attached to a substrate is:

$$\epsilon_{f,free} = -\alpha_{Tf} \Delta T \tag{15}$$

Where:

α_{Tf} is the linear thermal expansion coefficient of the film

If the film is attached to the substrate, the actual strain in the film must be equal to the strain of the substrate such that:

$$\epsilon_{f,attached} = -\alpha_{Ts} \Delta T \tag{16}$$

The thermal mismatch strain is defined as the difference between the actual strain and the strain the film would have if it was free [1]. This thermal mismatch strain is given as:

$$\varepsilon_{f,mismatch} = (\alpha_{Tf} - \alpha_{Ts}) \Delta T \tag{17}$$

المنارة للاستشارات
www.manaraa.com

The film achieves this biaxial strain by developing an in-plane biaxial stress. The in-plane biaxial stress only occurs when the two in-plane stress components are equal to each other. The biaxial stress is given as:

$$\sigma_{f,mismatch} = \frac{E}{1-v} \in_{f,mismatch} \quad (18)$$

Where:

E is the Young's Modulus of the film

v is the film's Poisson ratio

Note that a positive stress indicates a tensile stress and a negative value indicates compressive stress. The film stress will be positive if the thermal expansion coefficient of the film is greater than that of the substrate.

4.3 Background Equations on Center Deflection in a MEMS Structure

The center deflection associated with biaxial bending in a system fixed at both ends can be derived from fundamental beam equations. In this section, the formula for the center deflection is illustrated. This equation for a beam's center deflection will then be adapted to analyze the MEMS three-layer system.

Due to symmetry, analyzing half the beam is sufficient. Hence, in this study, a beam with half the membrane length, fixed at one end and free at the other will be considered. Figure 4.1 shows the center deflection when a system experiences negative curvature (beam deflects downwards).

المنارة للاستشارات

www.manaraa.com

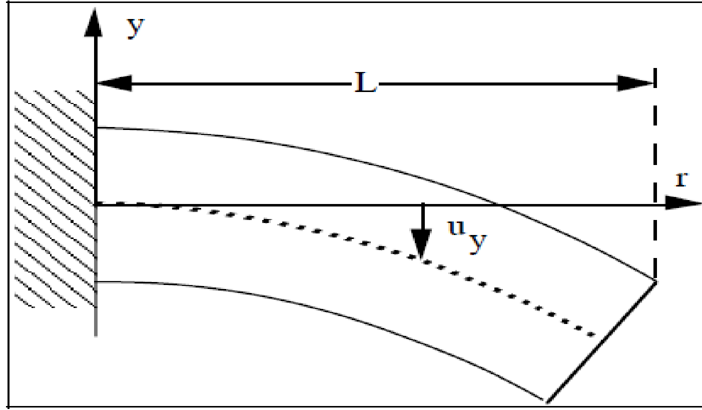

Figure 4.1: Negative Center Deflection of a Beam (u_y or δ) with Displacement along a Radius r, from Center. [12]

Equation (19) shows the relationship between center deflection and the beam curvature. The beam curvature is assumed constant for the pure bending case.

$$\frac{d^2u_y}{dr^2} = K = -\frac{(1-v_s)}{E_s}\frac{12M}{h^3} = constant \tag{19}$$

When equation (19) is integrated twice, one obtains:

$$u_y(r) = \frac{kr^2}{2} + c_1 + c_2 \tag{20}$$

Applying the boundary conditions:

$$\frac{du_y}{dr} = 0, u_y = 0, when\, r = 0$$

The constants c_1 and c_2 both vanish. Hence, we obtain:

$$u_y(r) = \frac{kr^2}{2} = -\frac{(1-v_s)}{E_s}\frac{12M}{h^3}\frac{r^2}{2} \tag{21}$$

At the edge of the beam, r = L. By substituting equation 7, we obtain the center deflection as:

$$u_y(r) = \delta = -\frac{(1-v_s)}{E_s}\frac{6M}{h^3}L^2 \tag{22}$$

المنارة للاستشارات
www.manaraa.com

Since $k = 1/\rho$, where ρ is the radius of curvature, by combining equations 19 and 22 the center deflection can be represented more conveniently as:

$$\delta = \frac{2L^2}{\rho} \tag{23}$$

4.4 Analysis of Center-Deflection in Multi-layer MEMS Devices Due to Thermal Stress

In this thesis, we will concentrate on the effects of thermally induced deflection in a device that is comprised of multiple thin layers of film. The originally developed Stoney equation [13] is commonly used to determine the residual stress of a thin film on a thick substrate. One important limitation of employing Stoney equation for membrane-based MEMS devices is that the derivation assumes film thickness to be negligible as compared to the substratrate thickness. Hsueh [32] recently developed an exact closed-form solution that calculates the overall radius of curvature for a multi-layer thin film structure for which there is no limitation on the thickness of each layer of film. Using Hsueh's method, there are always three unknowns to be solved and three boundary conditions that is to be satisfied regardless of the number of layers in a system. When a layer of thin film is deposited onto a layer of different material it is allowed to cool to room temperature. When cooled, the composite system is subjected to bending due to thermal expansion coefficient mismatch of the composite layer materials. The strain distribution in the system ε, can first be decomposed into two terms: the uniform strain component c, and the location of the bending axis, t_b. Note that the bending axis is defined as the line in the cross section of the system where the bending strain is zero, not

www.manaraa.com

the conventional neutral axis as described in the beam theory. Mathematically, the expression developed for the strain distribution in the system is given as:

$$\varepsilon = c + \frac{z - t_b}{r} \tag{24}$$

Where:

r: is the radius of curvature for the system

z: is the height of a thin film layer

The boundary conditions are as follows; the first states that the resultant force due to the uniform strain component is zero:

$$\sum_{i=1}^{n} E_i.(c - \alpha_i \Delta T)t_i = 0 \tag{25}$$

Where:

i: refers to each layer in the system

n: is the number of layers in the system

α: is the coefficient of thermal expansion

The second boundary condition is that the resultant force due to the bending strain component is zero:

$$\sum_{i=1}^{n} \int_{h_{i-1}}^{h_i} \frac{E_i (z - t_{b)}}{r} dz = 0 \tag{26}$$

Finally, the third boundary condition states that the sum of the bending moment with respect to the bending axis ($z=t_b$) is in equilibrium with the applied moment:

المنارة للاستشارات
www.manaraa.com

$$\sum_{i=1}^{n} \int_{h_{i-1}}^{h_i} \sigma_i (z - t_b) dz = M \tag{27}$$

Where:

M: is the applied moment per unit width of the multilayer

σ: is the normal stress in each layer of the film

When equations (25) to (27) are solved, the following would be obtained:

$$c = \frac{(\sum_{i=1}^{n} E_i t_i \alpha_i) \Delta T}{\sum_{i-1}^{n} E_i t_i} \tag{28}$$

$$t_b = \frac{E_1 t_1^{\ 2} + \sum_{i=2}^{n} E_i t_i (2h_{i-1} + t_i)}{2(E_1 t_1 + \sum_{i=2}^{n} E_i t_i)} \tag{29}$$

$$\frac{1}{r} = \frac{3[E_1 (c - \alpha_1 \Delta T) t_1^{\ 2} - \sum_{i=2}^{n} E_i t_i (c - \alpha_i \Delta T)(2h_{i-1} + t_i)] + 6M}{E_1 t_1^{\ 2} (2t_1 + 3t_b) + \sum_{i=2}^{n} E_i t_i [6h_{i-1}^{\ 2} + 6h_{i-1} t_i + 2t_i^{\ 2} - 3t_b (2h_{i-1} + t_i)]} \tag{30}$$

Where:

ΔT: is the temperature difference between the deposition temperature and the room temperature as the system is cooled.

t_i: is the thickness of each layer in the system

h: is the height of each film layer

The deflection δ, of the system as defined equation (23) is given as:

المنارة للاستشارات

www.manaraa.com

$$\delta = \frac{L^2}{2r}$$

Where:

L: is the length of the beam

Equation (30) gives the radius of curvature for any system with multiple layers of thin film. Note that for a bilayer strip that consists of a single thin film on a substrate, equation (30) reduces to Stoney's equation.

4.5 Center Deflection in a Three-layer System

The multilayer system that is being considered in this thesis consists of three layers, as that is the most commonly encountered configuration for membrane-based MEMS devices. One application that we will consider as a case study in this thesis is the MEMS capacitive micromachined ultrasonic transducers (CMUTs) that are used for ultrasonic imaging and other significant acoustic immersion applications [33-34]. The first layer of a CMUT membrane is silicon nitride (SIN_X) deposited at 250^0C by PECVD system. The second layer is a metal electrode, deposited using direct current (DC) sputtering at approximately 60^0C. The third and final layer is another layer of silicon nitride to protect the metal electrode, deposited using PECVD at 250^0C. The schematic of the multilayer system and the coordinate system is shown in figure 4.2 below.

المنارة للاستشارات
www.manaraa.com

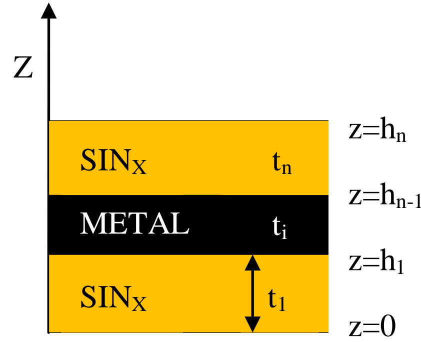

Figure 4.2: Schematic of Three-Layer SIN_X-Metal-SIN_X MEMS Structure

For the first layer, after the deposition at 250^0C, the system is cooled to room temperature (25^0C). Figure 4.3b shows the composite structure when a thin metal electrode is deposited onto the first nitride layer. As the composite structure is cooled to room temperature, there is a mismatch in thermal expansion coefficient between the metal and the silicon nitride layer. This will cause the metal to exert a tensile stress on the bottom silicon nitride layer, bowing the system down as shown in figure 4.3c. To obtain the first radius of curvature, the temperature is first considered to increase from 25^0C to 60^0C because the two layer system will be flat as shown in figure 4.3d. As the temperature is increased from 60^0C to 250^0C, the system will experience a compressive stress and will give the first radius for the two-layer membrane with a temperature difference ΔT, of 190^0C as shown in figure 4.4a. Silicon nitride is then deposited at 250^0C (figure 4.4b) to form the three-layer system. As the system is cool to room temp at 25^0C (figure 4.4c), thermal stress is induced in the system which causes the structure to deflect downwards for the temperature difference of -225^0C. This gives rise to the second

المنارة للاستشارات
www.manaraa.com

radius of curvature. Both these radius of curvature are superimposed to give the overall radius of curvature as shown in equation (30).

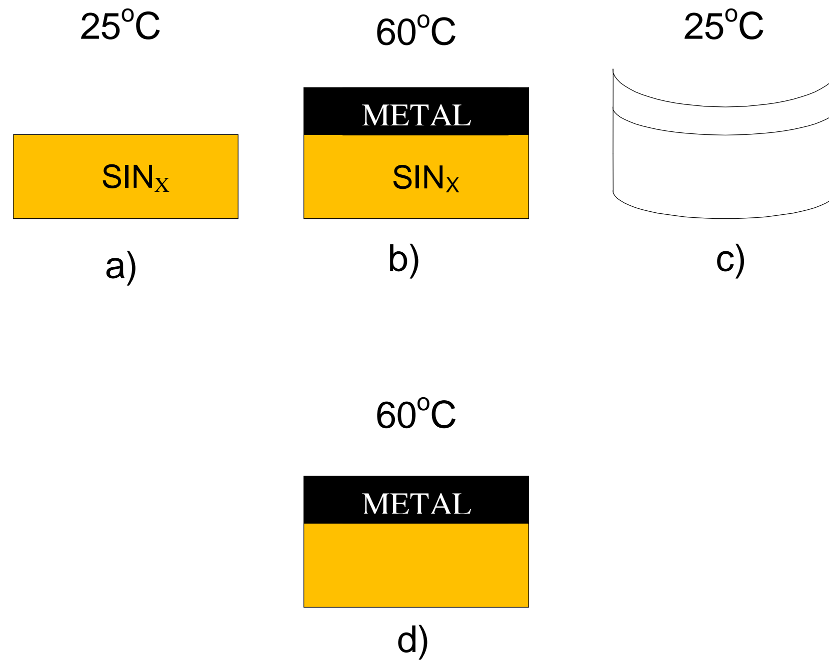

Figure 4.3(a-d): Thermal Steps of the First Two Layers of the Three-Layer System

المنارة للاستشارات
www.manaraa.com

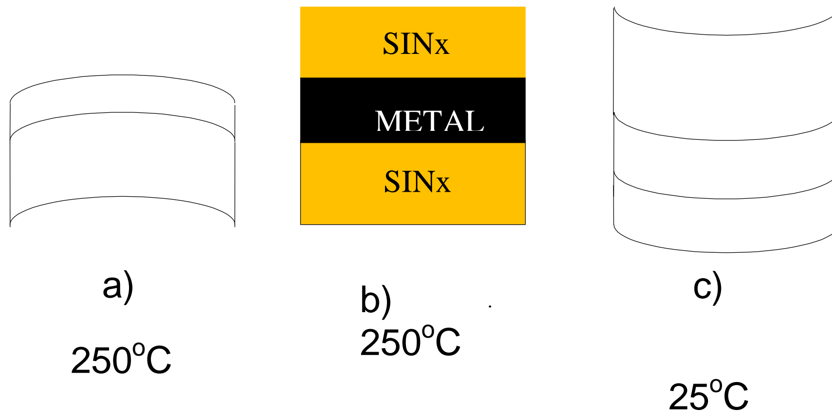

Figure 4.4: (a) Thermal Steps of the First Two Layers Along with Radius of Curvature, (b-c) the Complete Three-Layer System and its Radius of Curvature

4.6 Analytical Modeling of a Three-layer Nitride-Metal-Nitride Membrane

To analyze and design the three-layer system MEMS device, the Matlab® software was used to solve equations (23) and (28)-(30) simultaneously. As a reminder, the first radius of curvature is caused by the first layer of silicon nitride and the metal electrode (two layers) for a temperature difference of 190^0C. The second contributor was the entire three-layer system: the bottom silicon nitride layer, the metal electrode, and the top silicon nitride layer. As the system is cooled to room temperature from the deposition temperature, the temperature difference is -225^0C. The radii of curvatures were superimposed to give the equivalent radius of curvature for the system:

$$\frac{1}{r} = \frac{1}{r_1} + \frac{1}{r_2} \tag{31}$$

The membrane length for our analysis was 50 µm. This length was chosen as a reference, based on previous characterization of a micromachined capacitive transducer

المنارة للاستشارات
www.manaraa.com

[33-34]. The center deflection of the system is obtained from equation (23) where a beam length L, of 25µm was used.

4.6.1 Center Deflection and Thickness of Nitride Layer

In this first part of the analysis, an aluminum electrode with a constant thickness of 0.12 µm was chosen as the second layer in the three-layer system. The thickness of the bottom silicon nitride layer was varied for a specified top nitride layer thickness, and the center deflection was calculated. The results are summarized in figure 4.5. From this figure, the center deflection is minimized by increasing the bottom silicon nitride layer as compared to the top nitride layer. Note that in a MEMS device design, the total thickness of both nitride layers should be kept constant to keep the frequency response of the device constant. As an example, if a total nitride thickness (H1+H3) of 2 µm is desired, the center deflection is reduced by increasing the thickness of the bottom layer and decreasing the thickness of the top nitride layer (figure 4.5). It is important to note that, the deflection caused by the thermal expansion coefficient difference is only one of the considerations that need to be addressed in a device design. For instance, for a CMUT design with low operation voltage, high output pressure and sensitivity, one need to decrease the first nitride layer [33-34]. This conflict with the results obtained from the thermal stress analysis. Hence, a thorough investigation needs to be carried out to obtain optimum design parameters.

المنارة للاستشارات
www.manaraa.com

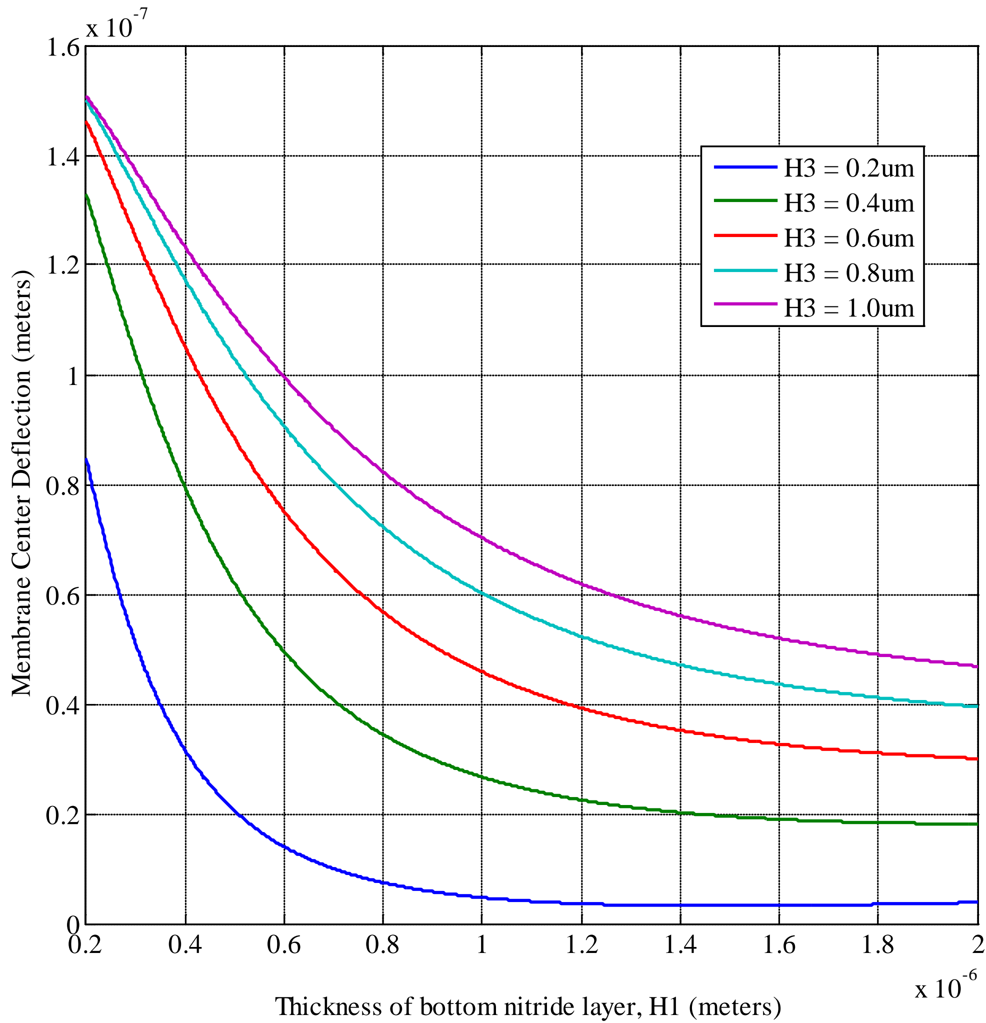

Figure 4.5: Center Deflection of a 50 µm Three-Layer System as a Function of Bottom Layer of Silicon Nitride for Different Thicknesses above the Metal Electrode (H3)

4.6.2 Effect of Metal Electrode Thickness on Membrane Center Deflection

In this section, the effect of the metal electrode thickness on the center deflection for the membrane is investigated. Aluminum was chosen for the metal electrode because it is widely available, inexpensive, and highly conductive. From equations (23) and (28)-(30), the thickness of the metal electrode is linearly proportional to the membrane curvature and hence, the membrane's deflection.

المنارة للاستشارات
www.manaraa.com

The thickness of both the bottom and top silicon nitride layers (H1 and H3 respectively) are taken as 0.8 µm. The membrane's center deflection as a function of metal electrode thickness is plotted in figure 4.6. From this figure, we observe that thinner metal layer is preferred in design to minimize the effect of thermal stress on the deflection of the membrane. However, there is a limit to the thickness of the electrode that is necessary for a device to be fully functional due to metal resistivity limitation.

المنارة للاستشارات
www.manaraa.com

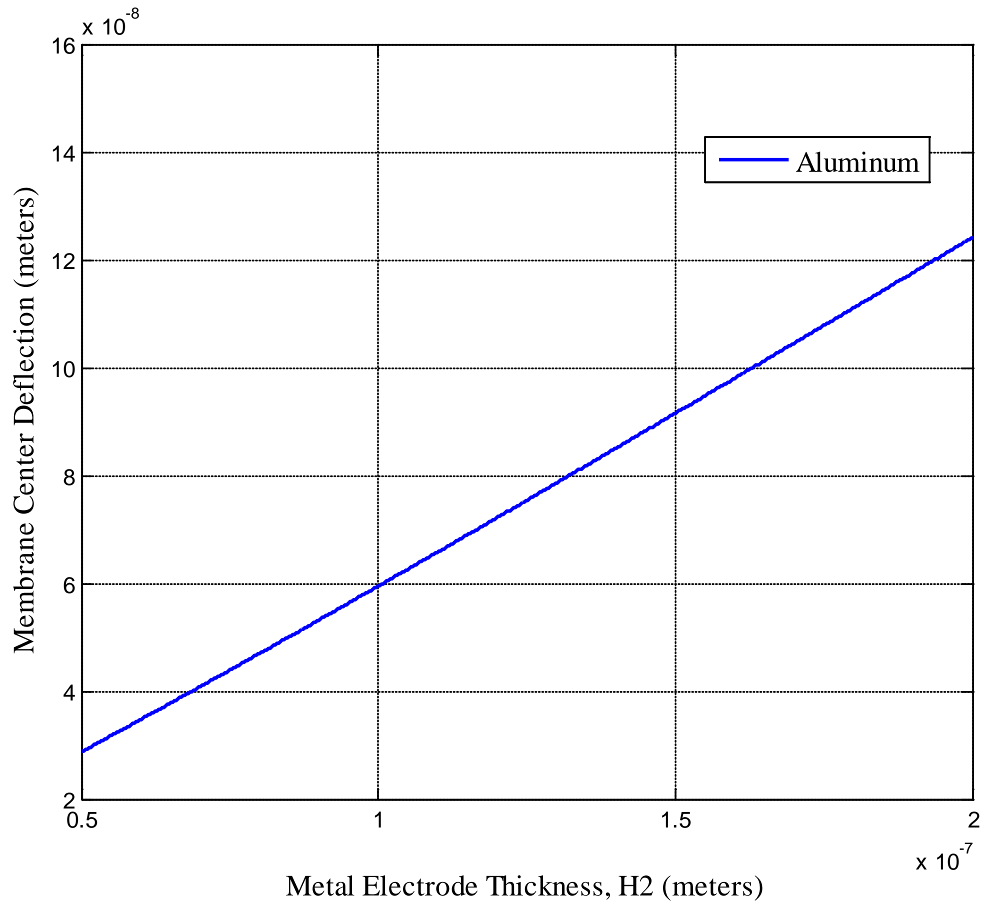

Figure 4.6: Center Deflection of a 50 μm Membrane as a Function of Metal Electrode Thickness

4.6.3 Effect of Thermal Expansion Coefficient on Center Deflection

In this section, different electrode materials were investigated for their effect on the center deflection of the membrane. The thickness of each metal was chosen as 0.12 μm and the material properties for the electrode materials are given in table 4.1.

المنارة للاستشارات
www.manaraa.com

Table 4.1: Thermal Expansion Coefficient and Resistivity of Different Metal Alternatives for Electrode in the Membrane. [1], [35-37]

	Aluminum (Al)	Gold (Au)	Platinum (Pt)	Tungsten (W)	Titanium (Ti)
Thermal Expansion Coefficient(10^{-6}/K)	23.1	14.2	8.8	4.5	8.6
Resistivity(10^{-8} Ω-m)	2.6	2.3	10.6	4.82	39
Young's Modulus (10^9 N/m^2)	69	78	168	411	116

From equations (23) and (30), the radius of curvature and the center deflection are directly proportional to the difference between the coefficient of thermal expansion of the metal electrode and the membrane material. This effect is shown below in figure 4.7.

المنارة للاستشارات
www.manaraa.com

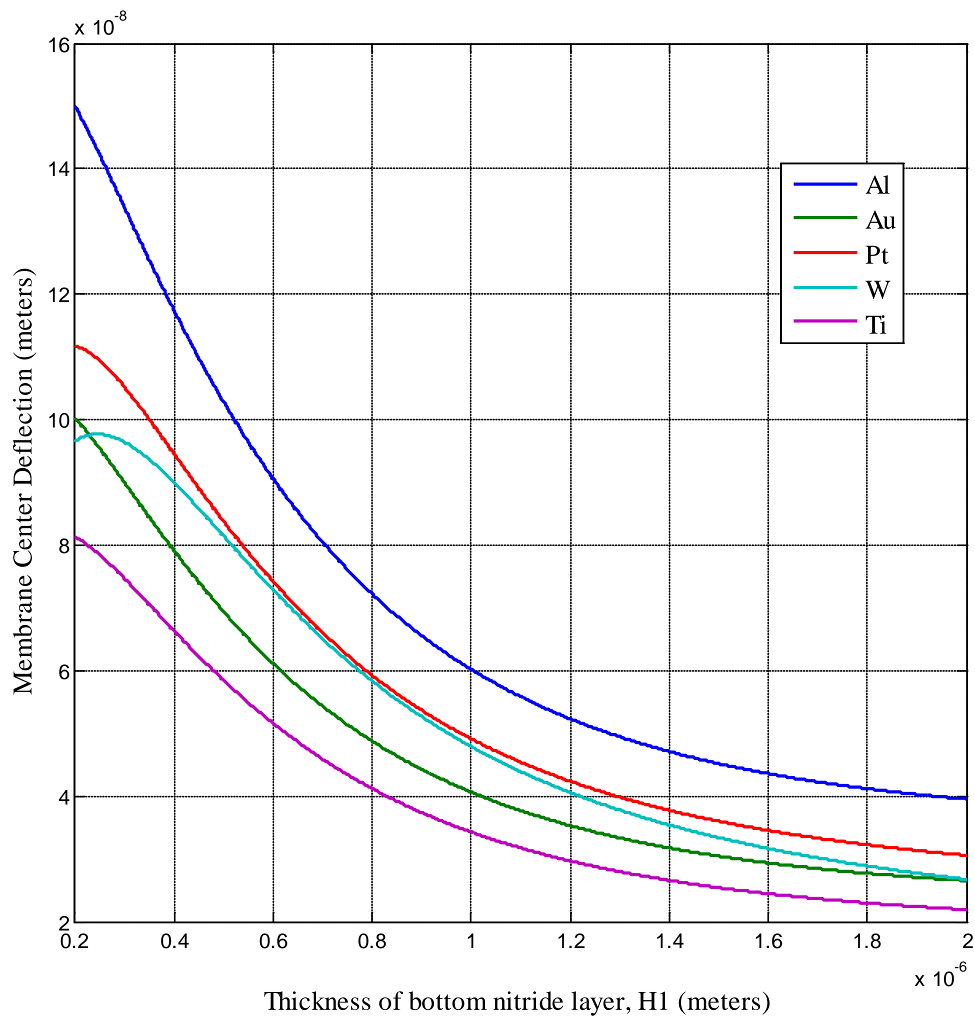

Figure 4.7: Center Deflection as a Function of Different Metal Alternatives with Constant Thickness

If we consider only the thermal expansion coefficients of the metal electrode, Titanium, Gold, Tungsten, and Platinum all reduce the thermal stress effects on the membrane. However, Tungsten for example (table 4.1) has a very large modulus of elasticity and may cause the membrane to be too stiff for certain applications. Most important though is that the resistivity of a metal determines its electrical conductivity.

www.manaraa.com

The electrical conductivity of a metal is defined as the reciprocal of the metal's resisitivity. A titanium electrode therefore, would be more likely to have a lower electrical conductivity than if gold was used (table 4.1). In addition, any capacitive MEMS device is adversely affected by the resistance of the top electrode. A high resistance can increase noise and loss in the system, thereby reducing sensitivity [33-34].

4.6.4 Thermal Expansion Coefficient with Normalized Electrode Thickness

The thicknesses of the different metal alternatives that were discussed in the preceding section should be normalized. This is done to obtain the same electrical conductivity that was attained from a 0.12 μm aluminum electrode. The effective metal thickness for each metal is obtained from the base material, Aluminum (Al) as follows:

$$eff.thickness\ of\ metal = \frac{Resistivity\ of\ metal}{Resistivity\ of\ Aluminum} \times Al\ thickness \qquad (32)$$

The resistivity and effective metal thickness for the different metal alternatives are given in table 4.2 below.

Table 4.2: Resistivity and Effective Metal Thickness for some Metal Alternatives. [36-39]

	Aluminum (Al)	Gold (Au)	Platinum (Pt)	Tungsten (W)	Titanium (Ti)
Resistivity (10^{-8} Ω-m)	2.6	2.3	10.6	4.82	39
Effective metal thickness (μm)	0.12	0.106	0.49	0.222	1.8

المنارة للاستشارات
www.manaraa.com

As can be seen in table 4.2, to obtain the same electric conductivity of a 0.12 µm thick aluminum electrode, platinum requires a thickness of almost 0.5 µm while titanium needs to be 1.80 µm. These two metals are therefore not optimum selections as shown in the metal thickness analysis (figure 4.6) where the membrane deflection increases with the thickness of the metal.

As illustrated in figure 4.8 below, Gold will serve as a good choice for a metal electrode within a membrane subjected to bow due to thermal stresses. Gold has a much lower thermal expansion coefficient and can give the same electric conductivity as aluminum with very low trade-off in thickness.

المنارة للاستشارات
www.manaraa.com

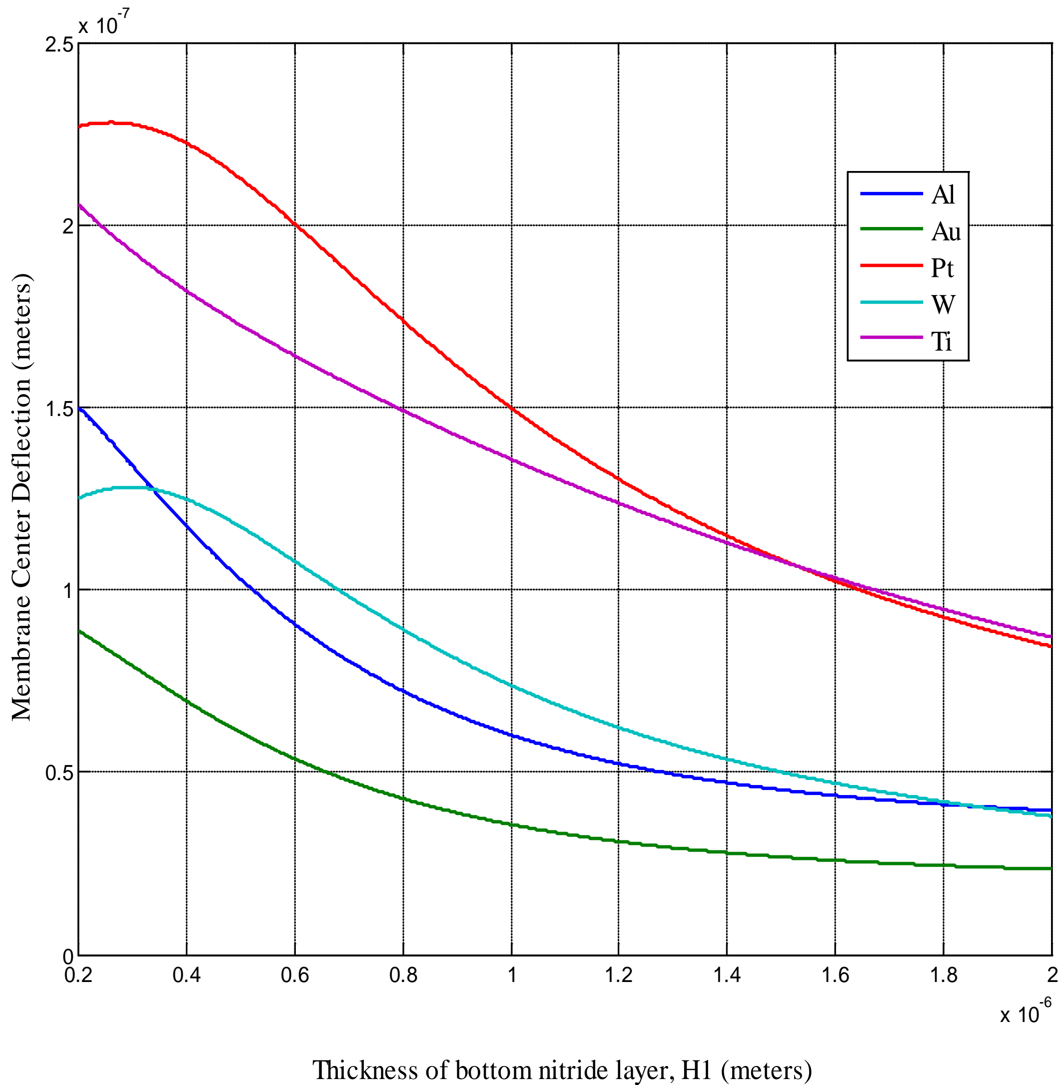

Figure 4.8: Center Deflection as a Function of the Different Metal Alternatives with Electrode Thickness Normalized for the Metal Electrical Conductivity

4.7 Curvature of a Thin Film on a Substrate Versus a Three-layer Membrane

The stress that a single layer of thin film exerts on a substrate was given in equation (10). Equation (10) can be re-arranged to give the film curvature as a function of the thickness of the film as:

المنارة للاستشارات
www.manaraa.com

$$K = t_f \frac{6\sigma(1-\nu)}{\mathrm{E}\, \mathrm{t_s}^2} \tag{33}$$

Where:

σ = stress in silicon nitride film after PECVD deposition

E = Young's Modulus of silicon substrate

ν = Poisson's ratio of silicon substrate

t_s = thickness of the substrate

t_f = thickness of the silicon nitride film

The film thickness and stress from four samples of silicon nitride that were deposited on silicon substrates using PECVD were taken and the values are shown in table 4.3. The average stress for four measurements was 32 MPa.

Table 4.3: Thickness and Thin Film Stress of Four Samples Deposited by PECVD

Thickness (nm)	Film Stress (MPa)
91	37.25
89	18.5
124	61.35
114	11.25

The substrate and film parameters in equation (33) were entered into Matlab®, to obtain the film curvature K, as a function of the film thickness t_f. The film thickness was varied from 80 nm (0.085 µm) to 130 nm (0.13 µm) and figure 4.9 shows the relationship between the film curvature and the thickness of the film.

المنارة للاستشارات
www.manaraa.com

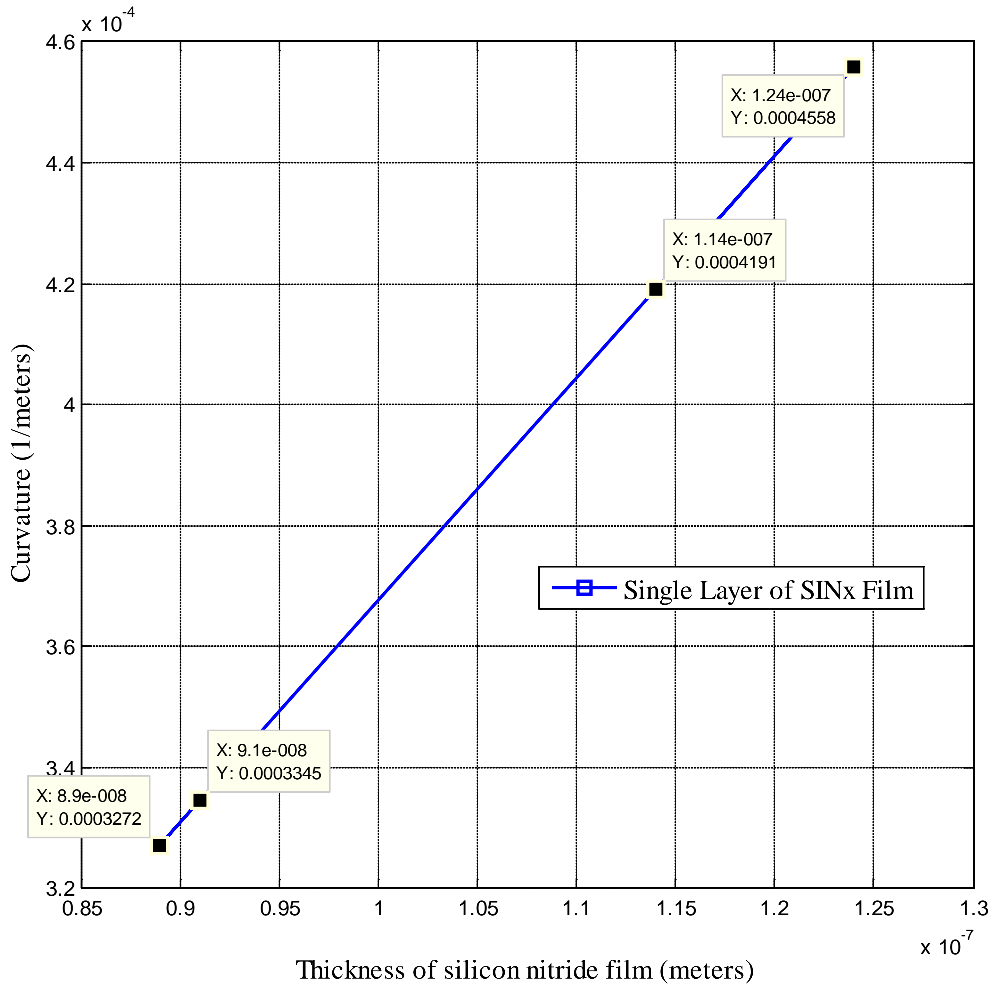

Figure 4.9: Curvature of Silicon Nitride Film as a Function of its Thickness on a Silicon Substrate

As can be seen from figure 4.9, the curvature of the silicon nitride film used on each substrate is on the order of 10^{-4} m^{-1}. The curvature also increases as the thickness of the nitride layer increase. A comparison of the curvature for the three-layer membrane and the curvature for a single layer of silicon nitride thin film deposited on a silicon substrate is illustrated in figure 4.10.

المنارة للاستشارات
www.manaraa.com

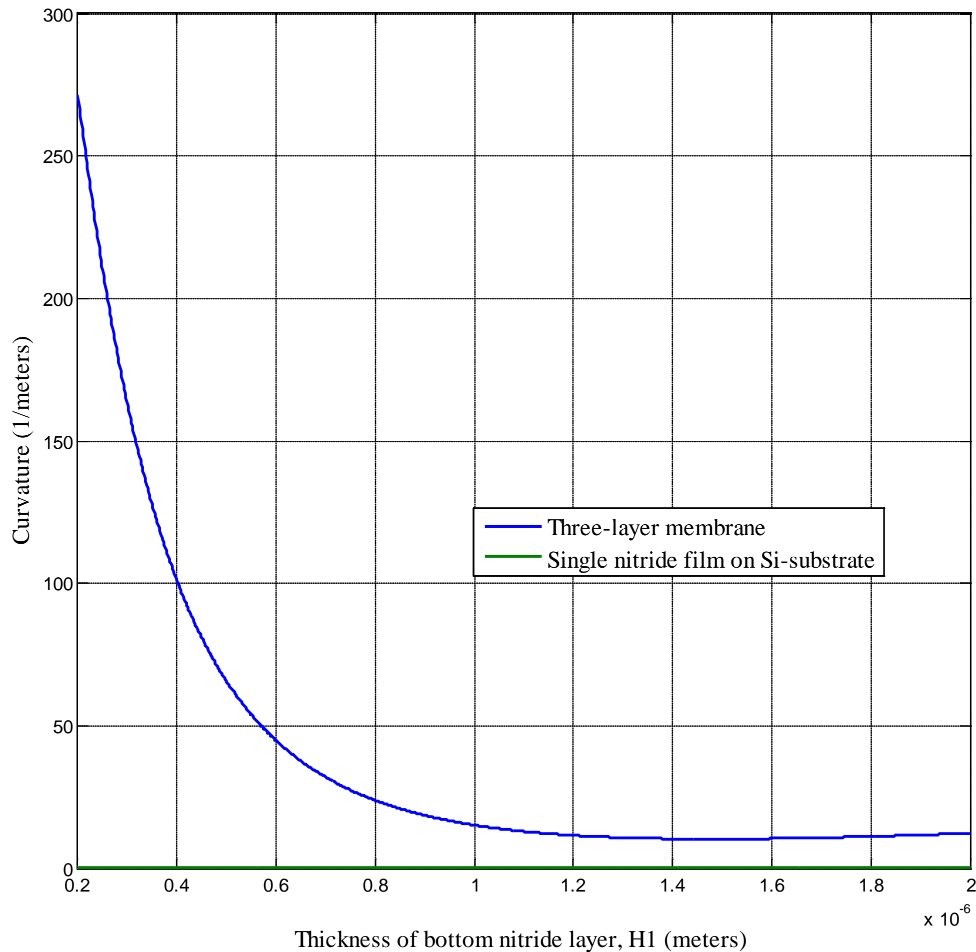

Figure 4.10: Curvature of Three-Layer Membrane (H2= 0.12 µm (Al), H3= 0.2 µm) and Single Nitride Layer on a Substrate, as a Function of Bottom Layer Thickness of the Membrane (H1).

For the three-layer membrane, the thickness of the second layer (metal) was chosen to be 0.12 µm for an aluminum electrode, and the top nitride layer was kept at a constant value of 0.2 µm. From figure 4.10, the curvature in the three-layer membrane is far more significant than in a single nitride film deposited on a silicon substrate. Even as the bottom layer thickness (figure 4.10) is pushed to the limit of 2 µm, the curvature of the single nitride film on silicon is still orders of magnitude lower than that of the three-

المنارة للاستشارات
www.manaraa.com

layer structure. Hence, among the three contributors to membrane bow, by far the thermal stress is the most significant contributor. However most of the studies simply ignore the thermal effect to the membrane bow in their analysis. Understanding and minimizing the effects of deflection due to thermal stress in membrane-based MEMS devices is therefore an important issue in micro-fabrication.

4.8 Conclusion

In chapter 4, a relationship between the thermal film stress and the center deflection in a MEMS devices was established. Based on analytical results, it was found that the thickness and the thermal expansion coefficient of each layer are important parameters for controlling the center deflection. The center deflection is reduced when each film have close thermal expansion coefficients. If a metal layer is needed for a particular structure, the electrical resisitivity of the metal is a useful parameter that can assist in selecting the appropriate material for minimum center deflection, hence optimized operation. Center deflection analysis is also of importance in the design of optical MEMS devices where particularly flat surfaces are needed.

المنارة للاستشارات
www.manaraa.com

CHAPTER 5: APPLICATIONS OF MEMBRANE-BASED MEMS DEVICES

5.1 Overview

In this chapter, some devices that incorporate the use of membrane-based MEMS structures will be discussed. These are presented to demonstrate the importance of the carried out study resulting in this thesis. In addition, a greater appreciation of the increasing use of membrane-based MEMS devices is conveyed.

The first part of the chapter will give some general examples of membrane-based MEMS devices in use today. The focus of the second part of the chapter will be on micromachined ultrasonic transducer technology. In particular, capacitive micromachined ultrasonic transducers (CMUTs) will be discussed. CMUTs are being studied by many researchers, and some current and intended future work by the author will be mentioned.

5.2 Common Membrane-based MEMS Devices

Some common examples of membrane-based MEMS devices, some of which are already in the industry today include MEMS Inertial Sensors, micro-mirrors, MEMS RF switches, and MEMS micro-resonators [1-3], [38].

5.2.1 MEMS Inertial Sensors

Inertial Sensors measures both translation (accelerometers) and rotational (gyroscopes) acceleration. Micro-accelerometers measure the variation of translational

المنارة للاستشارات
www.manaraa.com

speed such as acceleration, deceleration, and very rapid deceleration (shock). In an automobile, a micro-accelerometer is combined with an electronic circuit and is used to detect a shock and launch the airbag. Figure 5.1 below is a typical example of a micro-accelerometer, produced by an analog device.

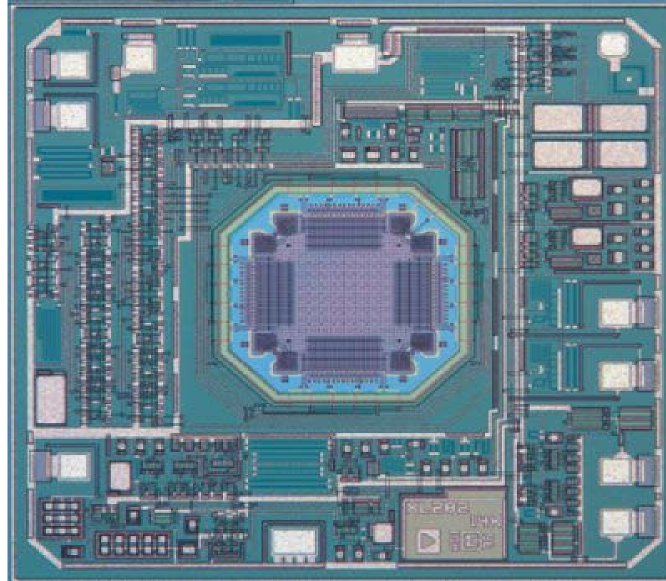

Figure 5.1: A Micro-accelerometer, ADXL Series, © Analog Devices Inc [38]

5.2.2 MEMS Micro-mirrors

MEMS Micro-mirrors have been the subject of study for many years and have recently become commercially available. The Digital Micro-mirror Device (DMD) developed by Texas Instruments uses a micro-mirror matrix for video display and is used as a high quality video projector.

Digital Light Processing (DLP) is a system made of a large matrix of micro-mirrors (DMD), and each mirror corresponds to a pixel. By the use of electrostatic actuation, the mirrors can change their angle of orientation. Therefore, when incident

المنارة للاستشارات
www.manaraa.com

light is directed on the matrix, the mirrors reflect a portion of the light to the screen, which depends on the orientation. Orientation angle therefore controls the luminance for each pixel. DLP is said to have advantages over Plasma, and LCD in terms of resolution and the best power ratio between light source and displayed light. The basic schematic of a DLP system is shown in the figure below and a MEMS digital micro-mirror device is shown in figure 5.3.

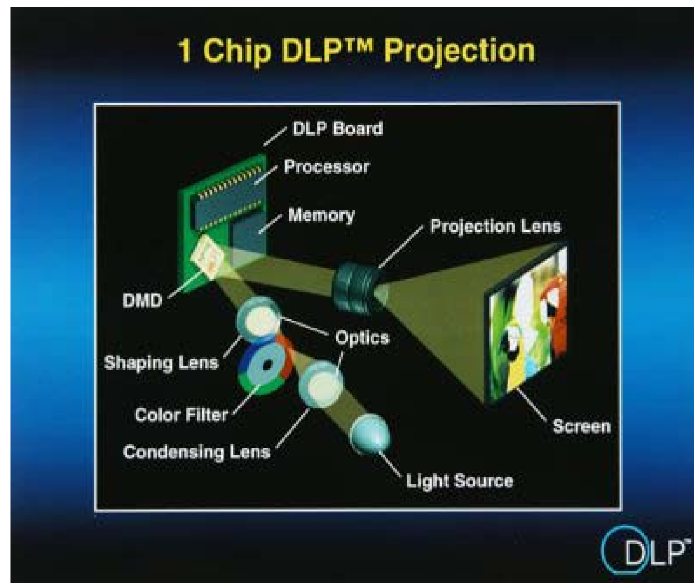

Figure 5.2: DLP Projection System with Single DMD Chip, © Texas Instrument Inc [38]

المنارة للاستشارات
www.manaraa.com

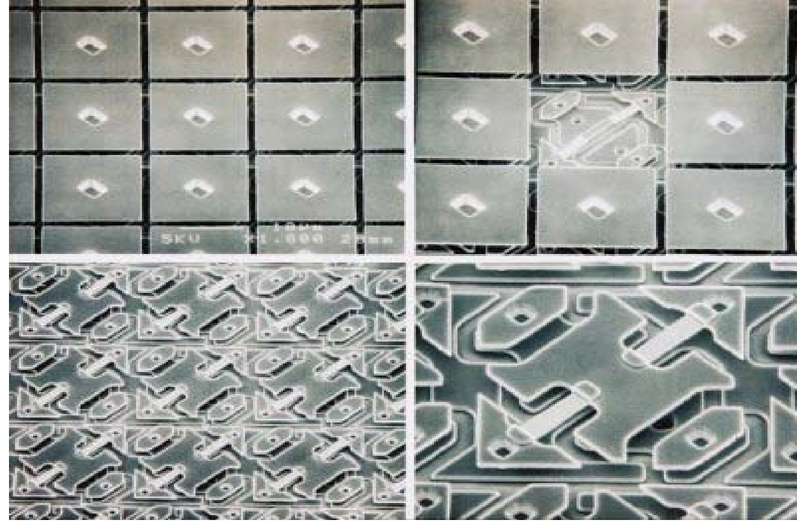

Figure 5.3: Digital Micro-mirror Device (DMD), © Texas Instrument Inc [38]

5.2.3 MEMS Micro-switch and Micro-Resonators

Probably the most common MEMS micro-switch that has been studied extensively is the MEMS radiofrequency (RF) switch. These are becoming quite popular and have the potential to replace full-electronic switches on applications where security, integration capabilities, and power consumption are critical.

Micro-Resonators are structures that vibrate instead of being displaced. They use mechanical vibrating parts to filter signals so that only one frequency, the Eigen frequency of the structure is kept. These can be used to replace electronic resonators and has application in electronic signal treatment where a back-and-forth conversion of electrical signal into mechanical stimulation is necessary. [3], [38]

Schematics of a typical MEMS micro-switch and a micro-resonator are shown in figure 5.4 and figure 5.5 respectively.

للاستشارات المنارة
www.manaraa.com

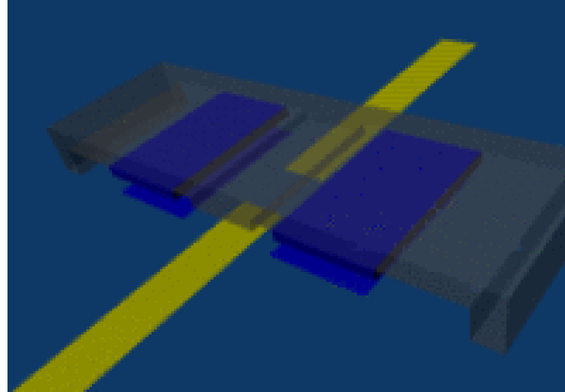

Figure 5.4: An Example of a MEMS RF Switch [38]

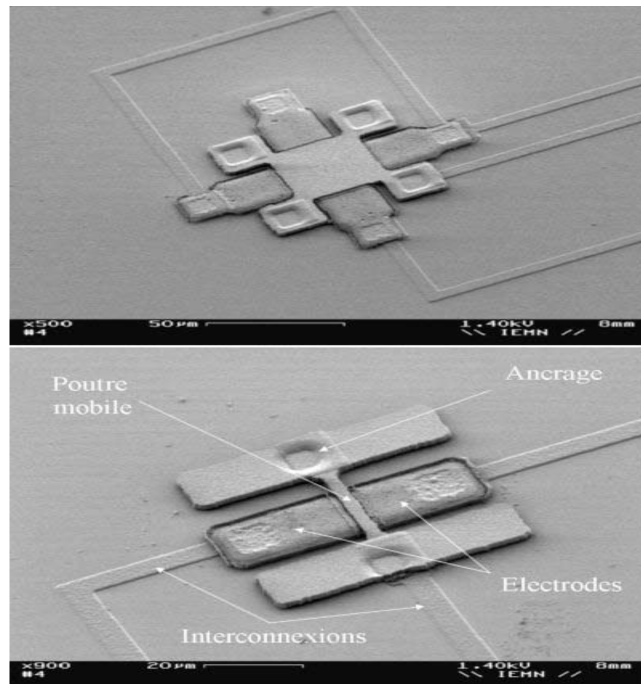

Figure 5.5: Micro-resonators Fabricated at the IEMN University in France [38]

5.2.4 MEMS Rotary Micro-motor

A promising area of research in the academic arena is the use of electrostatic actuation to develop rotating micro-motor devices. Figure 5.6 below is an example of a harmonic micro-motor developed by Mehregany et al.[39] where a rotor that turns in a

المنارة للاستشارات
www.manaraa.com

stator ring "wobbles" around some central axis as it turns. The idea is to basically create a central freely moving rotor with surrounding capacitive plates that when driven in the correct phase, allows the rotor to turn [3].

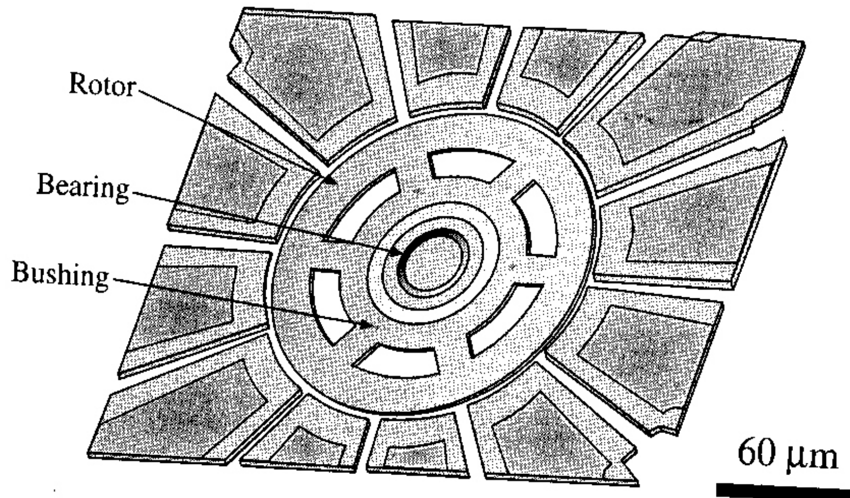

Figure 5.6: SEM Image of a Harmonic ("Wobble") Micro-motor [3], [39]

In an ideal case, the micro-motor device will operate by pure rolling without sliding or friction. Large electrostatic forces can also be generated as a result of the rotor coming closely to the stator [3]. The devices are usually fabricated from sacrificial oxide/polysilicon processes and have diameters in the range of 60-120 µm. Voltages as low as 26 V was used for operating the micro-motor that had an air-gap of 1.5 µm and excitation voltages as high 150 V was used across the same size air-gap [39]. This device has potential application in optical scanning as shown by Yasseen in [40].

للاستشارات المنارة
www.manaraa.com

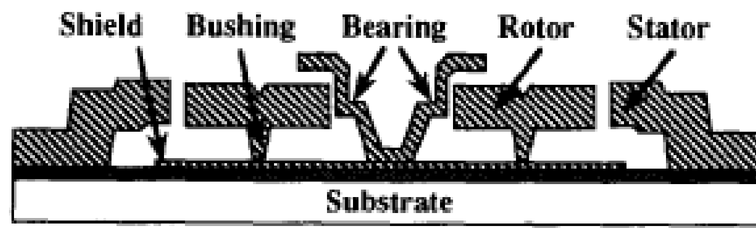

Figure 5.7: Cross-section of a “Wobble” Micro-motor with Heavily-Doped Polysilicon Shield [40]

5.2.5 MEMS Linear Micro-motors

Many MEMS linear micro-motor devices have been fabricated and the principle of electrostatic actuation has been used in their operation [41-43]. One example is the Scratch Drive Actuator [42] that uses a flexible conductive plate with a small bushing at one end and is capable of producing a defined linear motion. An example of the application of the Scratch Drive actuator (SDA) was developed by Fukuta et al. [43] where the SDA was used in conjunction with a reshaping technology to provide self-assembling to a 3-D polysilicon structure.

المنارة للاستشارات
www.manaraa.com

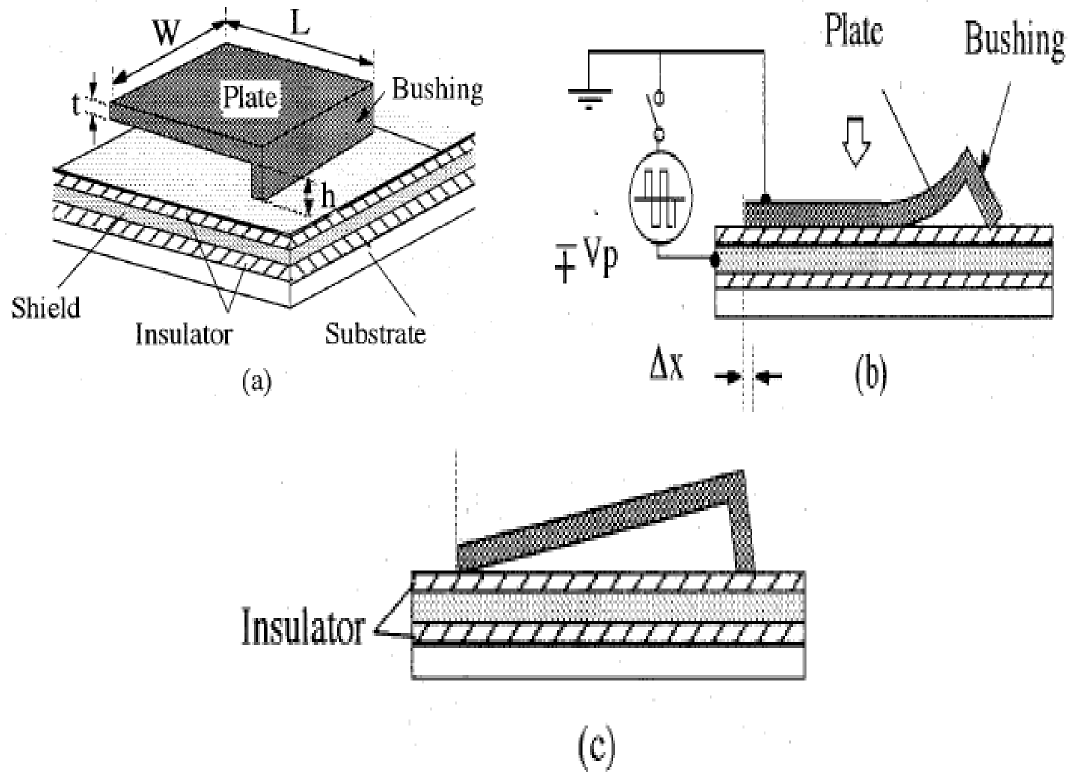

Figure 5.8: Scratch Drive Actuator Used in Self-Assembly of 3D Polysilicon Structure [43]

The plate will buckle down (figure 5.8b) when some voltage is applied between the buried conductor on the substrate and the plate, this causes the bushing to move forward by a small distance [3], [43]. A net movement of the plate will occur when the applied voltage is removed which is caused from friction between the bushing and the surface of the insulator.

5.2.6 MEMS Micro-grippers

MEMS Micro-grippers have the ability for handling micron-sized objects and have potential use in biomedical applications and microtelerobotics [44]. The micro-gripper discussed here is driven electrostatically by flexible, interdigited comb pairs and

المنارة للاستشارات
www.manaraa.com

have very small feature sizes. Polysilicon electrostatic micro-grippers have been successfully demonstrated by Kim et al. [44] and have been shown to achieve a 10 µm movement with an applied voltage of only 20 V (figure 5.9).

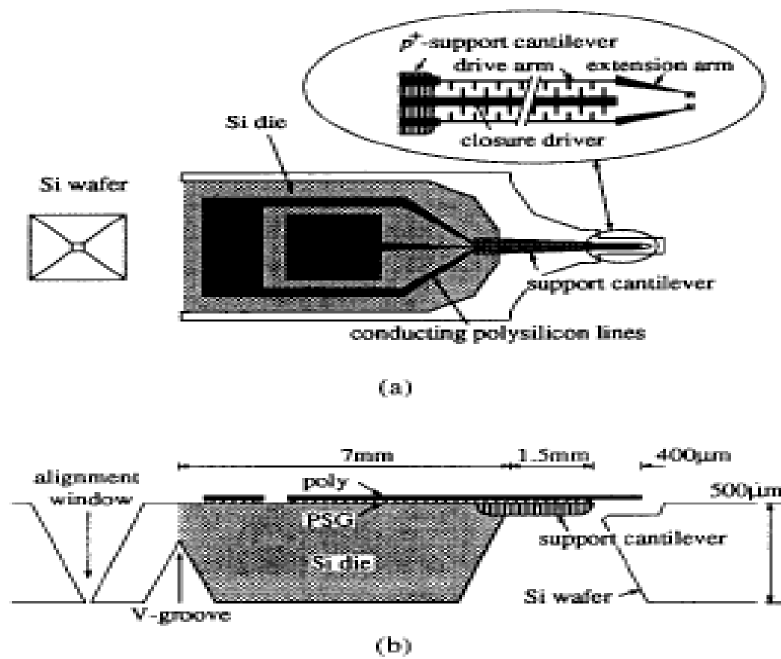

Figure 5.9: Electrostatic Micro-gripper (a) Top View, (b) Cross-sectional View [44]

5.3 Micro-machined Ultrasonic Transducers: An Overview

Ultrasonic Transducers are used to convert electrical energy into ultrasonic energy and vice versa. This conversion of energy can take place by use of different transduction mechanisms such as Piezoelectricity, Electrostatic, or Magnetostriction [3]. One of the main transduction mechanisms that have been useful in many large scale ultrasonic sensing devices are piezoelectric transduction. Piezoelectric transduction is based on the

المنارة للاستشارات
www.manaraa.com

piezoelectric effect which is the emission of charges from the surface of a material when a stress is applied [3].

Because the performance of bulk piezoelectrics is well known, thin film piezoelectrics were naturally adopted for the fabrication of micro-scale transducers. Some of the materials used as thin film piezoelectrics include: zinc oxide, lead zirconate titanate (PZT), piezoelectric ceramics and piezoelectric polymers [45-49]. The main problem with these materials though is that they have very high acoustic impedance as compared to that of the medium such as water or air necessitating the use of acoustic matching layers [50]. This results in lower operation bandwidth and reduced efficiency [51].

Alternative materials such as piezoelectric single crystals have been investigated but they are difficult to grow [52-53].

Capacitive Micromachined Ultrasonic Transducers (CMUTs) have various advantages to the current state-of-the-art piezoelectric transducer technology. An overview of the fabrication process of CMUTs and two potential applications will be the focus of the next sections in this chapter.

5.4 Capacitive Micromachined Ultrasonic Transducers (CMUTs)

5.4.1 Background

Capacitive Micro-machined Ultrasonic Transducers (CMUTs) were first developed at the Stanford University in the 1990's [51], [54].

المنارة للاستشارات
www.manaraa.com

Since the advent of CMUT technology, there has been extensive research about the design and modeling [55-66]; and the fabrication and experimental characterization of these MEMS-based ultrasonic devices [34], [67-72].

There have been successful array implementations by CMUTs [50], [73] and these have been shown to offer some advantage over their piezoelectric counterpart. These advantages include a higher bandwidth, and lower cost due to new fabrication techniques.

Some application areas where CMUTs have been found useful are in ultrasonic imaging [74-78], and for some micro-fluidic applications [79-80].

5.4.2 Operation of Capacitive Micromachined Ultrasonic Transducers (CMUTs)

The basic building block of a CMUT is a capacitor cell that consists of a metalized membrane with a moveable electrode (top electrode). This membrane is separated above a heavily doped silicon substrate (bottom electrode). Between the top and bottom electrode, there is an insulating layer (such as silicon nitride) which prevents the two electrodes from coming in contact. A single transducer element consists of many small capacitor cells that are connected in parallel, and many elements are used to make CMUT arrays [76-82].

The basic operation of the CMUT is described as follows: first, a DC voltage is applied between the metalized membrane and the substrate (bottom electrode). The membrane is attracted to the bulk by the electrostatic force, and induced stress in the membrane balances the attraction. The membrane is then set to vibrate and generates an

www.manaraa.com

ultrasonic wave when an AC voltage is applied to the electrode. Figure 5.10 below shows the basic setup of a single element of the transducer.

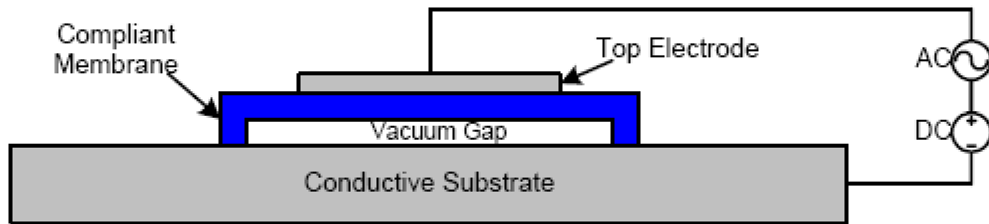

Figure 5.10: Schematic of a Single CMUT Transducer Element [80]

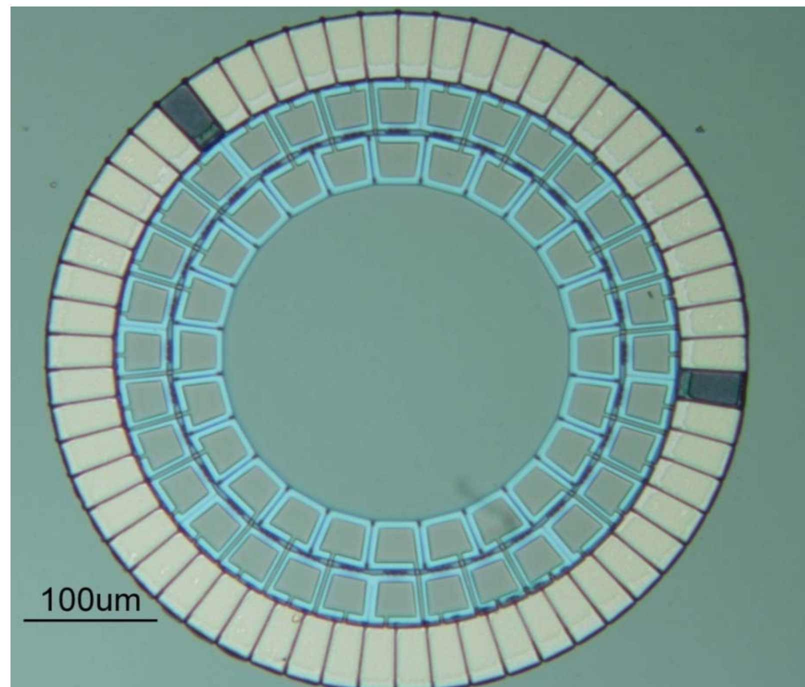

Figure 5.11: Annular Ring CMUT Fabricated with a Gap to Membrane Aspect Ratio of 1:1000 [81]

المنارة للاستشارات
www.manaraa.com

5.5 Fabrication of Capacitive Micromachined Ultrasonic Transducers

A capacitive micromachined ultrasonic transducer designed for a micro-fluidic application is shown in the schematic below.

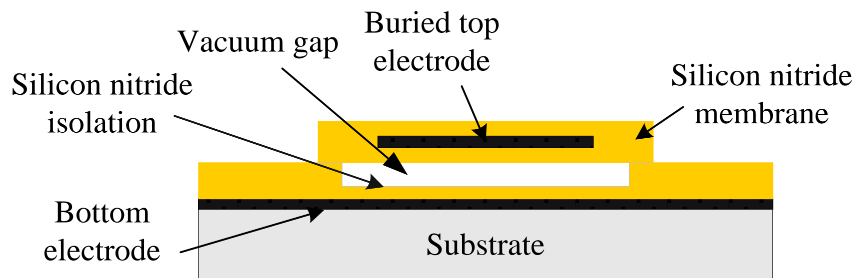

Figure 5.12: CMUT with Sealed Membrane Designed for Micro-fluidic Application [79]

Below is the summary of the process involved in fabricating a CMUT for an immersion application [34].

The surface micromachining process is a simple 5 mask process and requires the use of only three commonly used cleanroom equipments. These are a Plasma Enhanced Chemical Vapor Deposition (PECVD) deposition tool; a DC or RF metal sputtering station, and Reactive Ion Etch (RIE). A maximum process temperature of 250°C (during PECVD nitride deposition) enables the fabrication of CMUTs directly on top of CMOS electronics chip. This maximizes the area usage and increase the transducer performance by minimizing the parasitic capacitance.

The fabrication process flow is shown in figure 5.13 and the key information on each step is: (1) Bottom electrode Isolation: by deposition of low permittivity material, (2) Formation of bottom electrode; (3) Isolation of bottom electrode: deposition of low

المنارة للاستشارات
www.manaraa.com

permittivity PECVD silicon nitride; this protects the bottom electrode (aluminum) during the release of the sacrificial layer (chromium); (4) Formation of sacrificial layer: the sacrificial layer is used to form the gap that separates the membrane from the substrate; (5) Top electrode isolation formation: PECVD silicon nitride isolation is deposited to protect the top electrode (aluminum) during the release step; (6) Top electrode formation; (7) Membrane deposition: additional PECVD silicon nitride is deposited to increase the membrane thickness and to protect the top electrode from chromium etchant during the release step; (8) Membrane release: etch holes are placed along each corner of the membrane. After alignment, the silicon nitride is etched with an anisotropic Reactive Ion Etch (RIE) tool, and then the wafers are kept in chromium etchant for approximately 12 hours to form the gap; (9) Membrane sealing: the membranes are sealed for immersion applications, and to increase the membrane thickness to its design value by depositing an additional layer of silicon nitride in the PECVD station. During the silicon nitride deposition for the formation of the membrane in step 7, bondpads were also covered with silicon nitride. In the final step of the fabrication (not illustrated in Figure 5.13), the silicon nitride is etched in the RIE chamber to reveal the bondpads for final connection.

المنارة للاستشارات
www.manaraa.com

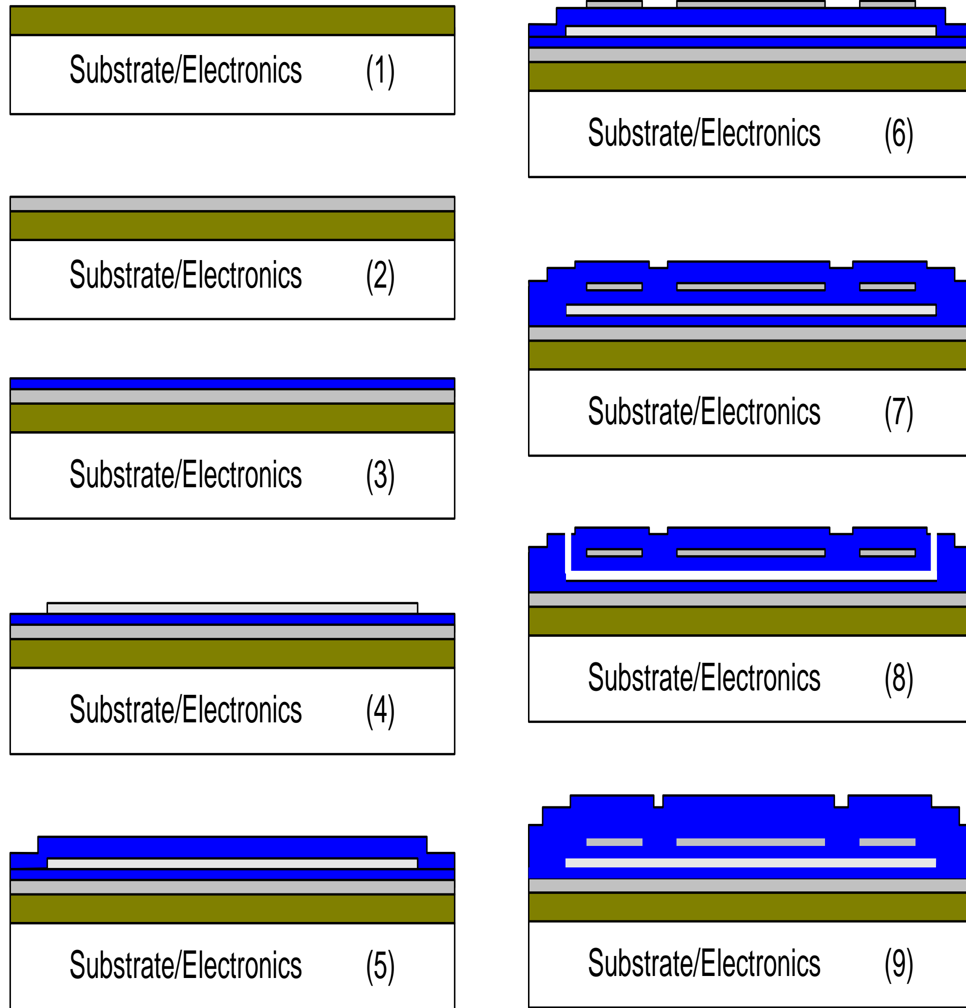

Figure 5.13: Illustration of the Fabrication Process Flow for a CMUT Designed for Immersion Application [34]

المنارة للاستشارات
www.manaraa.com

5.6 Future Work

Most of the future work will be tailored to the design of Capacitive Micromachined Ultrasonic Transducers. The use of a finite element modeling software such as ANSYS, will be used to compare the analytical results of the thermal stress discussed in chapter 4.

In addition, CMUTs will be fabricated directly at the University of South Florida state of the art Nanomanufacturing and Nanomaterials Research Center (NNRC). Diamond has recently been identified as a possible material for the CMUT membrane due to its good mechanical and electrical properties; and its ability to survive in harsh environments. These and other materials will be characterized and tested to broaden the spectrum of this new CMUT technology.

المنارة للاستشارات
www.manaraa.com

REFERENCES

1. S. D. Senturia, "Microsystem Design", © 2001 by Kluwer Academic Publishers

2. T-R. Hsu, "MEMS and Microsystems: Design, Manufacture, and NanoScale Engineering", 2nd Edition, copyright 2008 by John Wiley & Sons Inc

3. G.T.A. Kovacs, "Micromachined Transducers Sourcebook", copyright © 1998 by McGraw-Hill Companies, Inc

4. E. Sleeck, M. Shi, E. Kunnen, et al. "Optimization of Low Temperature Silicon Nitride Processes for Improvement of Device Performance", Microel. Reliability 45 (5-6) May-June 2005: pp. 865-868

5. J. M. Olson, "Analysis of LPCVD Process Conditions for the Deposition of Low Stress Silicon Nitride. Part I: Preliminary LPCVD Experiments", Materials Science in Semiconductor Processing 5(1) February 2002, pp. 51-60

6. T. J. Sanders, E.L. Caraway, C.J Hall, et.al. "Silicon Nitride Deposition Process for Low Cost Microelectronics Applications" Proc. Of the 12-th Bien. Univ./Govern./Ind. Microel. Symp. 20-23 July 1997, pp. 173-176

7. K. Peterson "Silicon as a Mechanical Material", Proc. of IEEE, vol. 70, No. 5, pp. 420-458, May 1982

8. D Virzonis, V Sinkevicius, V Grigaliunas, S Tamulevicius, R Kaliasas, "Advanced Process Equipment for PECVD silicon Nitride Deposition-an Experimental Study", ISSN 1392-1320, Materials Science (Medziagotyra). Vol. 12, No. 2, 2006

9. J Y M Lee, K. Sooriakumar, and M. M. Dange, "The Preparation, Characterization and Application of PECVD Silicon Nitride Films Deposited at Low Temperatures," Thin Solid Films, Vol. 203, pp. 275-287 (1991)

10. K D Mackenzie, B Reelfs, M W DeVre, R Westerman, and D J Johnson, "Characterization and Optimization of Low Stress PECVD Silicon Nitride for Production GaAs Manufacturing", Unaxis USA, Inc.

المنارة للاستشارات
www.manaraa.com

11. C. Iliescu, F E H Tay, and J Wei, "Low stress PECVD-SiN_x layers at high deposition rates using high power and high frequency for MEMS applications", Journal of Micromechanics and Microengineering, 16 (2006) pp. 869-874

12. W.D. Nix, "The Mechanical Properties of Thin Films", Department of Materials Science and Engineering, Stanford University, Jan. 2005

13. G. G. Stoney, Proc. R. Soc. London, Ser. A 82, 172, 1909

14. G.C.A.M. Janssen, et al., "Celebrating the 100th Anniversary of the Stoney Equation for Film Stress: Developments from Polycrystalline Steel Strips to Single Crystal Silicon Wafers", Thin Solid Films 517 (2009) pp. 1858-1867

15. http://www.edinformatics.com/math_science/states_of_matter.htm, "States of Matter", Accessed February 26th, 2009

16. J. Ashley Taylor, "The Mechanical Properties and Microstructure of Plasma Enhanced Chemical Vapor Deposited Silicon Nitride Thin Films", J. Vac. Sci. Technol. A 9 (4), July/Aug 1991, pp. 2464-2468

17. http://www.entrepix.com/Rudolph/AutoEL/AutoEL-3.html, "Rudolph Technology Auto EL III Ellipsometer", Accessed March 5, 2009

18. R.J Archer, "Determination of the Properties of Films on Silicon by the Method of Ellipsometry", J. Opt. Soc. Am. 52, pp.970-977 (1962)

19. M. Ghezzo, "Thickness Calculations for a Transparent Film from Ellipsometric Measurements", J. Opt. Soc. Am. 58, 368-378 (1968)

20. "Auto EL III Automatic Ellipsometer Instruction manual", Copyright 1962 Rudolph Research.

21. M.E Thomas, M.P. Hartnett, and J.E. Mckay, "The Use of Surface Profilometers for the Measurement of Wafer Curvature", Journal of Vacuum Science and Technology A: vol. 6, July 1988, pp. 2570-2571

22. M. Zecchino, and T. Cunningham, "Thin Film Stress Measurements Using Dektak Stylus Profilometers", Veeco Instruments Inc

23. W.D. Nix et al., "A Mechanism for Intrinsic Tensile Stresses in Thin Film", J. Mater. Res., 14 (8) 3467 (1999)

المنارة للاستشارات
www.manaraa.com

24. P. A. Flinn, D. S. Garter, and W. D Nix, "Measurement and Interpretation of Stress in Aluminum-Based Metallization as a Function of Thermal History", IEEE Trans. On Electron. Devices, vol. ED-34 no. 3, March 1987, pp. 689-699

25. D.J. Collins, A. J. Strojwas, D.D. White Jr., "A CFD Model for the PECVD of Silicon Nitride", IEEE Trans. On Semiconductor Manufacturing 7 (2) May 1994, pp. 176-183

26. D. L. Smith, A.S Alimonda, et. al, "Mechanism of SiN_xH_y Deposition From N_2-SiH_4 Plasma", J. Va. Sci. Technology B, vol. 8, Issue 3, May 1990, pp. 551-557

27. D. W. Hess, "Plasma-Enhanced CVD: Oxides, Nitride, Transition Metals, and Transition Metal Silicides", J. Vac. Sci. Technol., April-June 1984, pp. 244-252

28. B.S. Ramprasad and T.S. Radha, "Thermal Stress in Thin Films using Real-time Holographic Interferometry" International Conference on Holographic Systems, Components and Applications, Sept. 1989, pp. 29-32

29. W. Buckel, "Internal Stresses", Journal of Vacuum Science and Technology, Vol. 6, Issue 4, 1969, pp. 606-609

30. R. W. Hoffman, "Stress Distributions and Thin Film Mechanical Properties", Surface and Interface Analysis, Vol. 3, Issue 1, 1981, pp. 62-66

31. A.D. Yalcinkaya, H. Urey, at. al "Two-axis Electromagnetic Microscanner for High Resolution Displays", Journal of Microelectromechanical Systems, Vol. 15 No. 4, August 2006, pp. 786-794

32. C.H Hsueh, "Modeling of elastic deformation of multilayers due to residual stresses and external bending", J. of App. Phys., Vol. 91, No. 12, June 2002, pp. 9652-9656

33. R.O. Guldiken, J. McLean, and F.L. Degertekin, "CMUTs with Dual-electrode Structure for Improved Transmit and Receive Performance," *IEEE Trans. on UFFC*, 53, pp. 483-91, 2006

34. J. Knight, J. McLean, and F.L. Degertekin, "Low Temperature Fabrication of Immersion Capacitive Micromachined Ultrasonic Transducers on Silicon and Dielectric Substrates," *IEEE Transactions on Ultrasonics, Ferroelectrics and Frequency Control*, 51, pp. 1324-33, 2004

35. C. Liu, "Foundations of MEMS", copyright © 2006 Pearson Education, Inc.

المنارة للاستشارات
www.manaraa.com

36. G.V. Samsonov, Handbook of the Physicochemical Properties of the Elements, IFI-Plenum, New York, USA, 1968.

37. D.R. Linde, Handbook of Chemistry and Physics 75th Edition, CRC Press, London, UK, 1995

38. http://matthieu.lagouge.free.fr/mems/electrostatic.html, "Discovering MEMS and Microtechnology".

39. M. Mehregany et al, "Operation of Harmonic Side-Drive Micromotors Studied through Gear Ratio Measurements", Proc. Of Trans. 1991 Int. Conf. on Solid-State Sensors and Actuators, Jun. 1991, pp. 59-62

40. A.A. Yasseen, S.W Smith, M. Mehregany, and F.L Merat, "Diffraction Grating Scanners Using Polysilicon Micromotors", Proc. IEEE Micro Electro Mechanical Systems Conf., Jan-Feb 1995, pp. 175-180

41. W.S.N Trimmer, and K.J Gabriel, "Design Considerations for a Practical Electrostatic Micro-Motor", Sensors and Actuators, vol. 11, no. 2, Mar. 1987, pp. 189-206

42. T. Akiyama, and K. Shono, "Controlled Stepwise Motion in Polysilicon Microstructures", Journal of Microelectromechanical Systems, vol. 2, no. 3, Sept. 1993, pp. 106-110

43. Y. Fukuta, D. Collard, T. Akiyama, E.H Yang, and H. Fujita, "Microactuated Self-Assembling of 3D Polysilicon Structures with Reshaping Technology", Proc. 10th Annual Workshop of Micro Electro Mechanical Systems, Nagoya, Japan, Jan. 1997, pp. 477-481

44. C. J Kim, A. P Pisano, and R.S Muller, "Silicon-Processed Overhanging Microgripper", Journal Of Microelectromechanical Systems, Vol. 1, No. 1, Mar. 1992, pp. 31-36

45. C.E. Bradley, J.M. Bustillo, and R.M. White, "Flow Measurements in a Micromachined Flow System with Integrated Acoustic Pumping", Proceedings of 1995 IEEE Ultrasonic Symposium, (1995) pp. 505-510

46. A. Ballato, "Piezoelectricity: old effect, new thrusts," IEEE Trans. Ultrason., Ferroelect., Freq. Cont., vol. UFFC-42, Sep. 1995 pp. 916-926,

47. S. Fujishima, "The history of ceramic filters," IEEE Trans. Ultrasonic., Ferroelect., Freq. Cont., Vol UFFC-47, Jan.2000 pp. 1-7

المنارة للاستشارات

www.manaraa.com

48. E. Fukada, “History and recent progress in piezoelectric polymers,” IEEE Trans. Ultrason., Ferroelect., Freq. Cont., vol. UFFC-47, Nov. 2000 pp. 1277-1290

49. S.S. Foster et al “A history of medical and biological imaging with polyvinylidene fluoride (PVDF) transducers, “IEEE Trans. Ultrason., Ferroelect., Freq. Cont., vol. UFFC-47, Nov. 2000 pp. 1363-1371

50. X.C. Jin, I.O. Oralklan, F.L. Degertkin and B.T. Khuri-Yakub, “Characterization of One-dimensional Capacitive Micromachined Ultrasonic Immersion Transducer Arrays”, IEEE Trans. On UFFC, Vol. 48, (2001) pp. 750-760

51. M.I. Haller, and B.T. Khuri-Yakub, “A surface micromachined electrostatic air transducer”, in *Proc. IEEE Ultrason. Symp.,* Cannes, France, 1994, pp. 1241-1244

52. S.E. Park and T.R Shrout, “Characteristics of relaxor-based piezoelectric single crystals for ultrasonic transducers,” IEEE Trans. Ultrason., Ferroelect., Freq. Cont., vol. UFFC-44, Sep. 1997 pp. 1140-1147

53. C. G. Oakley and M. J. Zipparo “Single crystal piezoelectrics: a revolutionary development for transducers,” in Proc. IEEE Ultrason. Symp., 2000, pp. 1157 - 1167

54. H.T. Soh, I. Ladabaum, A. Atalar, C.F. Quate, and B.T. Khuri-Yakub, “Silicon Micromachined Ultrasonic Immersion Transducers”, Applied Physics Letters, Vol. 69, No. 24, (1996) pp. 3674-3676

55. P. Eccardt, K. Niderer, T. Scheiter, and C. Hierold, "Surface micromachined ultrasound transducers in CMOS technology," in *IEEE Ultrasonics Symposium*, 1996, pp. 959-62.

56. D. W. Schindel, D. A. Hutchins, L. C. Zou, and M. Sayer, "The design and characterization of micromachined air-coupled capacitance transducers," *IEEE Transactions on Ultrasonics Ferroelectrics and Frequency Control,* vol. 42, Jan 1995 pp. 42-50.

57. I. Ladabaum, X. C. Jin, H. T. Soh, A. Atalar, and B. T. Khuri-Yakub, "Surface micromachined capacitive ultrasonic transducers," *IEEE Transactions on Ultrasonics Ferroelectrics and Frequency Control,* vol. 45, May 1998 pp. 678-690.

58. A. Bozkurt, I. Ladabaum, A. Atalar, and B. T. Khuri-Yakub, "Theory and analysis of electrode size optimization for capacitive microfabricated ultrasonic transducers," *IEEE Transactions on Ultrasonics Ferroelectrics and Frequency Control,* vol. 46, Nov 1999 pp. 1364-1374.

المنارة للاستشارات
www.manaraa.com

59. O. Oralkan, X. C. Jin, F. L. Degertekin, and B. T. Khuri-Yakub, "Simulation and experimental characterization of a 2-D capacitive micromachined ultrasonic transducer array element," *IEEE Transactions on Ultrasonics Ferroelectrics and Frequency Control,* vol. 46, Nov 1999 pp. 1337-1340.

60. A. Caronti, G. Caliano, A. Iula, and M. Pappalardo, "An accurate model for capacitive micromachined ultrasonic transducers," *IEEE Transactions on Ultrasonics Ferroelectrics and Frequency Control,* vol. 49, Feb 2002 pp.159-168.

61. G. G. Yaralioglu, A. S. Ergun, B. Bayram, E. Haeggstrom, and B. T. Khuri-Yakub, "Calculation and measurement of electromechanical coupling coefficient of capacitive micromachined ultrasonic transducers," *IEEE Transactions on Ultrasonics Ferroelectrics and Frequency Control,* vol. 50, Apr 2003 pp. 449-456.

62. C. G. Yaralioglu, A. S. Ergun, and B. T. Khuri-Yakub, "Finite-element analysis of capacitive micromachined ultrasonic transducers," *IEEE Transactions on Ultrasonics Ferroelectrics and Frequency Control,* vol. 52, Dec 2005 pp. 2185-2198.

63. A. Ronnekleiv, "CMUT array modelling through free acoustic CMUT modes and analysis of the fluid CMUT interface through Fourier transform methods," *IEEE Transactions on Ultrasonics Ferroelectrics and Frequency Control,* vol. 52, Dec 2005 pp. 2173-2184

64. A. Lohfink and P. C. Eccardt, "Linear and nonlinear equivalent circuit modeling of CMUTs," *IEEE Transactions on Ultrasonics Ferroelectrics and Frequency Control,* vol. 52, Dec 2005 pp. 2163-2172.

65. S. Olcum, M. N. Senlik, and A. Atalar, "Optimization of the gain-bandwidth product of capactive micromachined ultrasonic transducers," *IEEE Transactions on Ultrasonics Ferroelectrics and Frequency Control,* vol. 52, Dec 2005 pp. 2211-2219.

66. D. Certon, F. Teston, and F. Patat, "A finite difference model for CMUT devices," *IEEE Transactions on Ultrasonics Ferroelectrics and Frequency Control,* vol. 52, Nov 2005 pp. 2199-2210.

67. X. C. Jin, I. Ladabaum, F. L. Degertekin, S. Calmes, and B. T. Khuri-Yakub, "Fabrication and characterization of surface micromachined capacitive ultrasonic immersion transducers," *IEEE Journal of Microelectromechanical Systems,* Vol. 8, 1999 pp. 100-14.

المنارة للاستشارات
www.manaraa.com

68. J. Knight and F. L. Degertekin, "Capacitive micromachined ultrasonic transducers for forward looking intravascular imaging," in *IEEE Ultrasonics Symposium*, 2002, pp. 1052-5.

69. O. Ahrens, A. Buhrdorf, D. Hohlfeld, L. Tebje, and J. Binder, "Fabrication of Gap-optimized CMUT," *IEEE Transactions on Ultrasonics Ferroelectrics and Frequency Control,* Vol. 49, Sep 2002 pp. 1321-1329.

70. E. Cianci, L. Visigalli, V. Foglietti, G. Caliano, and M. Pappalardo, "Improvements toward a reliable fabrication process for CMUT," *Microelectronic Engineering,* Vol. 67-68, 2003 pp. 602-608.

71. Y. L. Huang, A. S. Ergun, E. Haeggstrom, M. H. Badi, and B. T. Khuri-Yakub, "Fabricating capacitive micromachined ultrasonic transducers with wafer-bonding technology," *Journal of Microelectromechanical Systems,* Vol. 12, Apr 2003 pp. 128-137.

72. A. Caronti, A. Savoia, G. Caliano, and M. Pappalardo, "Design, fabrication and characterization of a capacitive micromachined ultrasonic probe for medical imaging," *IEEE Transactions on Ultrasonics Ferroelectrics and Frequency Control,* vol. 52, Nov 2005 pp. 2039-2046.

73. O. Oralkan, A. S. Ergun, J. A. Johnson, M. Karaman, U. Demirci, K. Kaviani, T. H. Lee, and B. T. Khuri-Yakub, "Capacitive micromachined ultrasonic transducers: next-generation arrays for acoustic imaging?," *IEEE Transactions on Ultrasonics Ferroelectrics and Frequency Control,* Vol. 49, Nov 2002 pp. 1596-1610.

74. O. Oralkan, A. S. Ergun, C. H. Cheng, J. A. Johnson, M. Karaman, T. H. Lee, and B. T. Khuri-Yakub, "Volumetric ultrasound imaging using 2-D CMUT arrays," *IEEE Transactions on Ultrasonics Ferroelectrics and Frequency Control,* Vol. 50, Nov 2003 pp. 1581-1594.

75. U. Demirci, A. S. Ergun, O. Oralkan, M. Karaman, and B. T. Khuri-Yakub, "Forward-viewing CMUT arrays for medical Imaging," *IEEE Transactions on Ultrasonics Ferroelectrics and Frequency Control,* Vol. 51, Jul 2004 pp. 887-895

76. F. L. Degertekin, R. O. Guldiken, and M. Karaman, "Micromachined capacitive transducer arrays for intravascular ultrasound," in *Proc. SPIE MOEMS Display and Imaging Systems III, San Jose, Ca*, 2005, pp. 104–114.

المنارة للاستشارات
www.manaraa.com

77. F. L. Degertekin, R. O. Guldiken, and M. Karaman, "Annular-ring CMUT arrays for forward-looking IVUS: Transducer characterization and imaging," *IEEE Transactions on Ultrasonics Ferroelectrics and Frequency Control,* vol. 53, Feb 2006 pp. 474-482.

78. D. T. Yeh, O. Oralkan, I. O. Wygant, M. O'Donnell, and B. T. Khuri-Yakub, "3-D ultrasound imaging using a forward-looking CMUT ring array for intravascular/intracardiac applications," *IEEE Transactions on Ultrasonics Ferroelectrics and Frequency Control,* vol. 53, Jun 2006 pp. 1202-1211.

79. H. Jagannathan, G.G. Yaralioglu, A.S. Ergun, F.L. Degertekin, and B.T. Khuri-Yakub, “Micro-fluidic Channels with Integrated Ultrasonic Transducers”, Proceedings of 2001 IEEE Ultrasonic Symposium, (2001) pp. 859-862

80. J. Mclean, and F.L. Degertekin, “Interdigital Capacitive Micromachined Ultrasonic Transducers for Sensing and Pumping in Micro-fluidic Applications”, Proc. Int. Conf. on Solid-state Sensors, Actuators, and Microsystems, (2003) pp.915-918

81. R. Guldiken J. Zahorian, M. Balantekin, F.L. Degertekin, C. Tekes, A. Sisman, and M. Karaman, “ Dual-Annular-Ring CMUT Array for Forward-Looking IVUS Imaging”, 2006 IEEE Ultrasonic Symposium, pp. 698-701

82. R. O. Guldiken, J. Zahorian, G. Gurun, M. S. Qureshi, M. Balantekin, C. Tekes, M. Karaman, S. G. Carlier, and F. L. Degertekin, "Forward-Looking IVUS Imaging Using a Dual-Annular Ring CMUT Array: Experimental Results," in *IEEE Ultrasonics Symposium*, 2007, pp. 1247-1250

المنارة للاستشارات
www.manaraa.com

APPENDICES

المنارة للاستشارات
www.manaraa.com

Appendix A: Sample MathLab® Code used for Calculating Center Deflection

```
for (a=1:1:5)

//Film Parameters//

E1=110e9;

E2=69e9;

H1=linspace(0.2e-6,2e-6,1000);

H2=0.12e-6

H3=0;

alpha1=8e-7;

alpha2=23.1e-6;

E3=110e9;

alpha3=8e-7;

deltaT1=190;

deltaT2=-225;


A=6.*(E2.*H1.*H2+H2.*H2.*E2+E3.*H3.*(H1+2.*H2+H3)).*E1.*H1.*(alpha2-
alpha1);

B=6.*(E2.*H3.*H2+H2.^2.*E2+E1.*H1.*(H1+2.*H2+H3)).*H3.*E3.*(alpha3-alpha2);

C=E1.*H1.*E2.*H2.*(4.*H1.*H1+4.*H2.*H2+6.*H1.*H2);

D=E2.*H2.*E3.*H3.*(4.*H1.*H1+4.*H3.*H3+6.*H3.*H2);

E=E1.*H1.*E3.*H3.*[4.*H1.*H1+4.*H3.*H3+6.*H1.*H3+12.*H2.*(H1+H2+H3)];
```


المنارة للاستشارات

www.manaraa.com

Appendix A (Continued)

```
F=E1.*H1.*H1+H2.*H2.*E2+E3.*H3.*H3;
//Calculates first curvature//
RAD1=(A+B).*deltaT1./(C+D+E+F);
H3=0.2e-6*a;
A=6.*(E2.*H1.*H2+H2.*H2.*E2+E3.*H3.*(H1+2.*H2+H3)).*E1.*H1.*(alpha2-
alpha1);
B=6.*(E2.*H3.*H2+H2.^2.*E2+E1.*H1.*(H1+2.*H2+H3)).*H3.*E3.*(alpha3-alpha2);
C=E1.*H1.*E2.*H2.*(4.*H1.*H1+4.*H2.*H2+6.*H1.*H2);
D=E2.*H2.*E3.*H3.*(4.*H1.*H1+4.*H3.*H3+6.*H3.*H2);


E=E1.*H1.*E3.*H3.*[4.*H1.*H1+4.*H3.*H3+6.*H1.*H3+12.*H2.*(H1+H2+H3)];
F=E1.*H1.*H1+H2.*H2.*E2+E3.*H3.*H3;
//Calculates second curvature//
RAD2=(A+B).*deltaT2./(C+D+E+F);


//Sum curvatures to find total//
RAD=RAD1+RAD2;
//Calculates Center Deflection//
if (a==1)
def1=0.5*RAD*(25e-6)^2;
end
```


المنارة للاستشارات
www.manaraa.com

Appendix A (Continued)

```
if (a==2)
def2=0.5*RAD*(25e-6)^2;
end
if (a==3)
def3=0.5*RAD*(25e-6)^2;
end
if (a==4)
def4=0.5*RAD*(25e-6)^2;
end
if (a==5)
def5=0.5*RAD*(25e-6)^2;
end
end
//Plot Center Deflection//
plot(H1,def1,H1,def2,H1,def3,H1,def4,H1,def5)
```


المنارة للاستشارات
www.manaraa.com